



FACULTY OF ELECTRICAL ENGINEERING
UNIVERSITY OF BANJA LUKA

ELECTRONICS

FACULTY OF ELECTRICAL ENGINEERING UNIVERSITY OF BANJA LUKA

Address: Patre 5, 78000 Banja Luka, Bosnia and Herzegovina

Phone: +387 51 211824

Fax: +387 51 211408

Web: www.etfbl.net

ELECTRONICS

Web: www.electronics.etfbl.net

E-mail: electronics@etfbl.net

Editor-in-Chief:

Branko L. Dokić, Ph. D.

Faculty of Electrical Engineering, University of Banja Luka, Bosnia and Herzegovina

E-mail: branko.dokic@etfbl.net

Co Editor-In-Chief:

Prof. Tatjana Pešić-Brdanin, University of Banja Luka, Bosnia and Herzegovina

E-mail: tatjanapb@etfbl.net

International Editorial Board:

- Prof. Goce Arsov, St. Cyril and Methodius University, Macedonia
- Prof. Zdenka Babić, University of Banja Luka, Bosnia and Herzegovina
- Prof. Petar Biljanović, University of Zagreb, Croatia
- Prof. Milorad Božić, University of Banja Luka, Bosnia and Herzegovina
- Prof. Octavio Nieto-Taladriz Garcia, Polytechnic University of Madrid, Spain
- Dr Zoran Jakšić, IHTM, Serbia
- Prof. Vladimir Katić, University of Novi Sad, Serbia
- Prof. Tom J. Kazmierski, University of Southampton, United Kingdom
- Prof. Vančo Litovski, University of Niš, Serbia
- Dr Duško Lukač, University of Applied Sciences, Germany
- Prof. Danilo Mandić, Imperial College, London, United Kingdom
- Prof. Bratislav Milovanović, University of Niš, Serbia
- Prof. Vojin Oklobdžija, University of Texas at Austin, USA
- Prof. Predrag Pejović, University of Belgrade, Serbia
- Prof. Ninoslav Stojadinović, University of Niš, Serbia
- Prof. Robert Šobot, Western University, Canada
- Prof. Slobodan Vukosavić, University of Belgrade, Serbia
- Prof. Volker Zerbe, University of Applied Sciences of Erfurt, Germany

Secretary:

Mladen Knežić, M.Sc.

Željko Ivanović, M.Sc.

Publisher:

Faculty of Electrical Engineering, University of Banja Luka, Bosnia and Herzegovina

Number of printed copies: 100

Strained Silicon Layer in CMOS Technology

Tatjana Pešić-Brđanin, Branko L. Dokić

Abstract— Semiconductor industry is currently facing with the fact that conventional submicron CMOS technology is approaching the end of their capabilities, at least when it comes to scaling the dimensions of the components. Therefore, much attention is paid to device technology that use new technological structures and new channel materials. Modern technological processes, which mainly include ultra high vacuum chemical vapor deposition, molecular beam epitaxy and metal-organic molecular vapor deposition, enable the obtaining of ultrathin, crystallographically almost perfect, strained layers of high purity. In this review paper we analyze the role that such layers have in modern CMOS technologies. It's given an overview of the characteristics of both strain techniques, global and local, with special emphasis on performance of NMOS biaxial strain and PMOS uniaxial strain. Due to the improved transport properties of strained layers, especially high mobility of charge carriers, the emphasis is on mechanisms to increase the charge mobility of strained silicon and germanium, in light of recent developments in CMOS technology.

Index Terms—Strained silicon layers, uniaxial strain, biaxial strain, CMOS technology.

Review Paper

DOI: 10.7251/ELS1418063P

I. INTRODUCTION

IN the last 30 years, the primary characteristic of improving performance of CMOS technology has been scaling the dimensions of the components. Continuous reduction in size of devices and simultaneously increase of the size of chips has led to the production of highly complex integrated circuits with ultra large scale of integration. The realization of such complex high-speed integrated circuits is enabled by using CMOS technology with critical dimensions of components of a few nanometers. Numerous factors influence the increase of speed of MOS transistor operation; the most important is the time of the carriers transport through the channel under the gate, which can be reduced by shortening the gate length.

However, the other demands of designing integrated circuits with ultra large scale of integration, such as, for example, the increase in density on the chip and reducing the size of the chip, have led to the scaling of other transistor dimensions. Fig. 1 shows the trend of reducing the gate length that has led to the emergence of new technologies [1]. Reducing the gate length caused a simultaneous scaling of other technological parameters, in order to meet the required performances of integrated circuits regarding high speed and low power consumption, or the desired degree of integration. However, with recent CMOS technologies, in which the gate length is less than 90 nm, this performance improvement becomes more difficult due to physical limitations in miniaturization of MOS transistors.

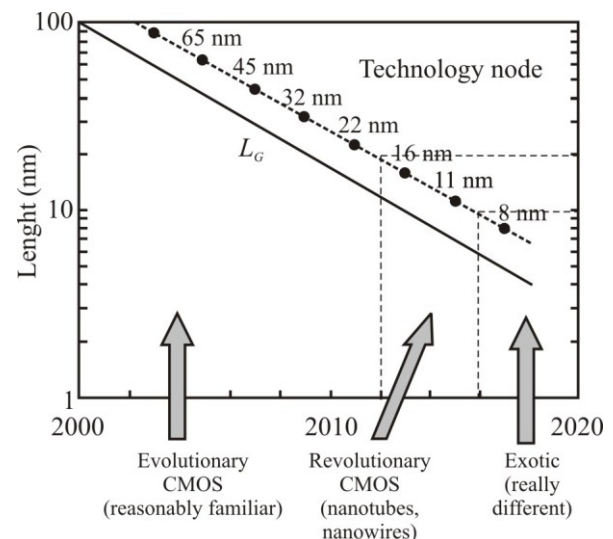


Fig. 1. Technology and gate length evolution [1].

With the scaling dimensions, at the same time, new process technologies were developed, especially ultra high vacuum chemical vapor deposition (UHV-CVD), and molecular beam epitaxy (MBE), which enabled the obtaining of ultrathin, crystallographically almost perfect, strained layers of high purity. Due to the low temperature processes ($<600^{\circ}\text{C}$), diffusion of impurities is very weak. This allowed obtaining of super abrupt pn junctions with much greater difference in concentration of ingredients on both sides of the joint than in the case of other epitaxial growth techniques. Using the metal-organic CVD (MO-CVD) growth techniques, the

Manuscript received 15 December 2014.

Tatjana Pešić-Brđanin is with the Faculty of Electrical Engineering, University of Banja Luka, Banja Luka, Bosnia and Herzegovina (phone: +387-51-221-829; fax: +387-51-211-408; e-mail: tatjanapb@etfbl.net).

Branko L. Dokić is with the Faculty of Electrical Engineering, University of Banja Luka, Banja Luka, Bosnia and Herzegovina (phone: +387-51-221-824; fax: +387-51-211-408; e-mail: bdokic@etfbl.net).

homogeneous and heterogeneous layers are created with controlled concentration and thickness up to 50 Å, while using the MBE technology obtained layers were even less than 10 Å of thickness [2]. With these new technological processes, and great progress in lithographic techniques, new structures of MOS transistors with ultrathin layers of germanium or SiGe alloys on silicon substrates were reached. Compared to conventional, these new structures are characterized, above all, with a significantly higher speed operation, as well as improved current-voltage performances. The operations of these transistors, however, are characterized by a number of new physical phenomena (quantum effects, transport across the heterojunction, ballistic transport, tunneling etc.), which must be taken into account in optimization of such structures and specifications of their electrical characteristics [3,4].

One of the new technological structures of MOS transistors, the structures with strained silicon in channel region, thanks to advances in the local strain technique, are used in CMOS technology (e.g., logic circuits in 90 nm CMOS technology) [5]. The increase of the carrier mobility, which is implemented by appropriate silicon strain, provides higher speed of the carriers, respectively higher current drive, under the same conditions of polarization and a fixed oxide thickness. On the other hand, it means that with the same current conditions in the channel, thicker oxides and/or lower voltages supply could be used, which leads to relaxation of compromise between the current, consumption and the effects of short channels. Therefore, the strain technique and a corresponding increase in carrier mobility are considered as factors required for future CMOS technologies [6,7].

This paper provides an overview of the principles and application techniques of strained layers, with special emphasis on the physical mechanisms to increase mobility due to strain, in modern and future CMOS technologies.

II. PHYSICAL MECHANISMS FOR MOBILITY ENHANCEMENT

One way to improve the performance of MOS transistor is the possibility to change the properties of materials. The property of silicon to exhibit modified characteristics of transport parameters while strained [8,9] is used for this purpose. Measurements which were performed on Hall structures in strained silicon layer at room temperature showed a large electron mobility, which in the case of a very low temperatures (0.4 K) reaches extremely high values, up to 500 000 cm²/Vs [10]. The increase in electron mobility in strained silicon layers is supported by theoretical studies [11,12].

A. Electron Mobility Enhancement

The silicon layer straining is technologically commonly performed by the growth of silicon on the SiGe substrate. Fig. 2 schematically shows the crystal structure of the silicon and the relaxed layer of Si_{1-x}Ge_x. Since the lattice constant of Si_{1-x}Ge_x composition is higher than the silicon lattice constant in the balance state, the pseudomorph layer of silicon which has grown on the relaxed Si_{1-x}Ge_x layer (or virtual substrate) is under biaxial strain. The distance of silicon atoms assimilate to the higher atomic distance in the SiGe layer, thereby

increasing the lattice constant of silicon a_{Si} in the growing level. The lattice constant of the SiGe composition, and hence the strained silicon, is approximately a linear function of the germanium content (or the value of the x in the Si_{1-x}Ge_x composition). As the germanium lattice constant is about 4% higher than the lattice constant of silicon, it will, for example, Si_{0.75}Ge_{0.25} virtual substrate cause an increase in lattice constants of strained silicon which has grown on the composite layer for approximately 1% [9].

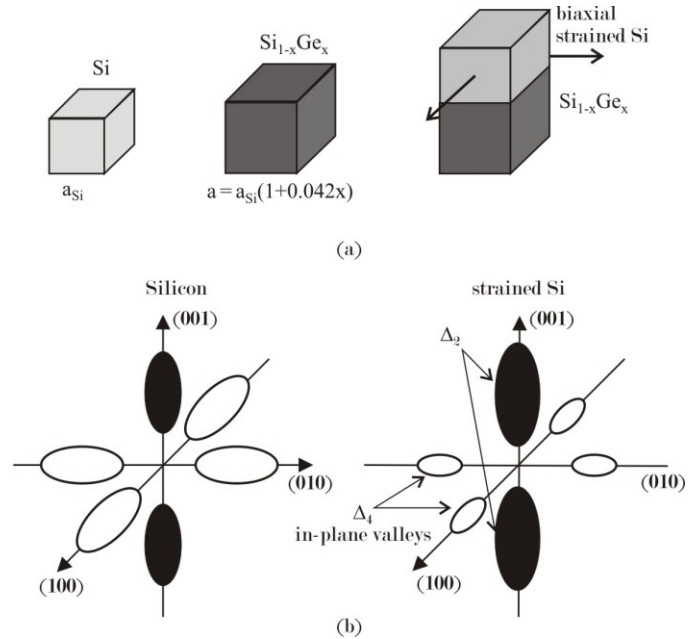


Fig. 2. Schematic illustration of balance silicon structure in SiGe composition (a) and conduction zones of unstrained and strained silicon (b).

The strain leads to the shape degeneration of six equipotential valleys in conduction zone by reducing the value of the energy minimum in the two transverses (Δ_2), compared to the values of the energy minimum in four longitudinal directions (Δ_4) [13] (Fig. 2). The result is an effective anisotropy of the electron effective mass; transversal mass ($m_t = 0.19m_0$) appears, and it is smaller than the longitudinal mass ($m_l = 0.916m_0$). m_0 is the electron mass. Table 1 shows the values of the electron effective mass depending on the crystallographic planes and directions for silicon and germanium [14].

The difference of the effective mass causes different physical properties in Δ_2 and Δ_4 valleys. The conductive electron mass in parallel MOS interface is smaller in Δ_2 the plane than in the Δ_4 plane, and, therefore, the electron mobility is greater in the Δ_2 plane, than in the Δ_4 plane. Also, as the inverted layer thickness and the subzone energy are determined by effective mass in the direction normal to MOS interface, an inversion layer is thinner and the subbands energy is lower in Δ_2 plane, and so the effective mass is higher.

The effect of strain on the electron mobility can be reflected by changing the subbands energy, i.e. the energy levels in the conduction zone. The increase of the energy of the sublevels results in increased mobility through two mechanisms: increasing the average value of mobility in Δ_2 plane due to a large number of electrons with higher mobility and modification of the bottom of the conduction band leads to a reduction of dissemination of holders on the phonons, which, in total, increases the electron mobility even when the electric field has low values [13].

TABLE I
ELECTRON EFFECTIVE MASS DEPENDING ON THE CRYSTALLOGRAPHIC PLANES AND DIRECTIONS FOR SILICON AND GERMANIUM

	Plane	Channel direction	Effective mass ($\cdot m_0$)		
			m_x	m_y	m_z
Silicon	(100)	$\langle 001 \rangle$	0.19	0.19	0.916
		$\langle 011 \rangle$			
	(110)	$\langle 001 \rangle$	0.19	0.553	0.315
		$\langle 110 \rangle$	0.553	0.19	
Germanium	(100)	$\langle 001 \rangle$	0.153	0.153	
		$\langle 011 \rangle$	0.085	1.12	0.12
	(110)	$\langle 001 \rangle$	0.601	0.082	
		$\langle 110 \rangle$	0.082	0.601	

Unlike the conduction band, the structure of the valence band is similar for silicon and germanium. The energy minimum and maximum are located in the same crystallographic directions. Band structure of germanium is less anisotropic when compared to silicon, so its effective mass is lower. Germanium structure reacts to strain in a similar way as silicon structure, with improved response to the strain inversion.

There are several empirical phrases to assess the width modification of the band gap zone of strained silicon. For strained silicon, a narrowing of the band gap zone depending on the percentage of germanium in the relaxed $\text{Si}_{1-x}\text{Ge}_x$ layer can be calculated:

$$E_{g\,st} = E_g - 0.4 \cdot x \quad (\text{eV}) \quad (1)$$

where E_g is the silicon bang gap energy, and $E_{g\,st}$ is the strained silicon bang gap energy.

Of particular importance is the electron mobility model which has to include the functional mobility dependence for strain, temperature, ingredients concentration in the channel and polarization. Fig. 3.a shows the experimental results for mobility enhancement factor, which is defined as the mobility ratio of strained and unstrained silicon. The findings for the two models of mobility, derived mainly from the theory of phonon diffusion, are also shown [3,15,16].

Figure 3.b shows the dependence of effective mobility on

the effective electric field at a room temperature, with and without strain. It shows that the mobility enhancement factor is almost unchanged in a wide range of values for the external electric field.

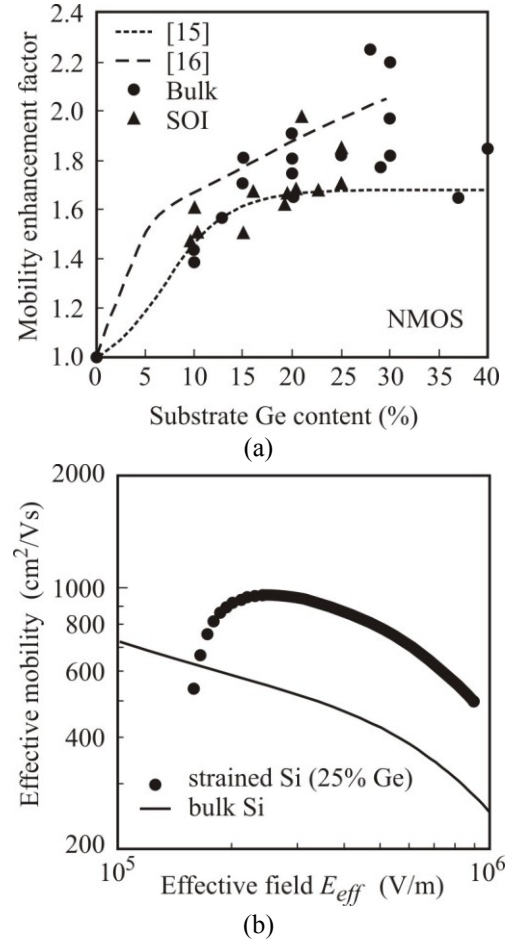


Fig. 3. Mobility enhancement factor as a function of Ge content in SiGe substrates for NMOS transistor (a) and effective field dependence of electron mobility in biaxial strained Si NMOS (b).

B. Hole Mobility Enhancement

Unlike the electron mobility enhancement, the physical mechanisms of change of the hole mobility in PMOS transistors due to strain have not been fully explained. Also, it has been shown that the effects of the uniaxial and biaxial strain on the hole mobility are completely different. With the biaxial strain, the hole mobility enhancement due to strain is a consequence of the decrease of the hole effective mass in the occupied zones of the valence zone, suppression of inter-subband scattering and increase of the availability of subbands with a smaller effective mass, i.e. higher mobility.

Figure 4.a shows the experimental results for hole mobility enhancement factors for biaxial strained PMOS transistor, and the results obtained by theoretical models. It can be noted that a large percentage of germanium significantly increase the hole mobility. The dependence of hole mobility enhancement factors on the effective electric field indicates to the fact that the maximum hole mobility enhancement factor is at a lower

values E_{eff} , Figure 4.b. As mobility at large values E_{eff} is significant for most practical applications, it is necessary to use a biaxial strain silicon layers with a high content of germanium. Recent studies have shown that, when uniaxial compression along $\langle 110 \rangle$ PMOS channel direction is applied, the hole mobility enhancement factors is higher, even for less strain, and it does not decrease significantly with increasing values E_{eff} [17-20].

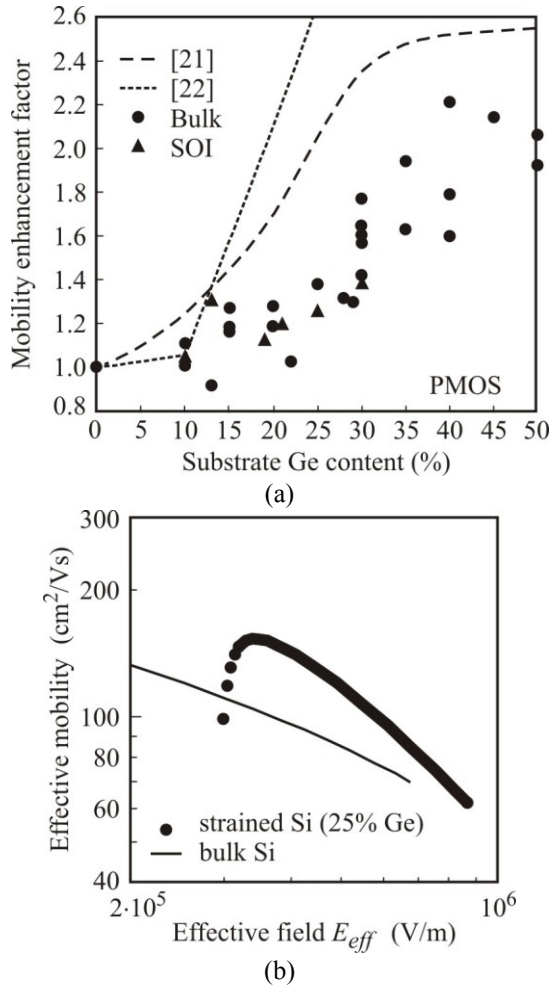


Fig. 4. Mobility enhancement factor as a function of Ge content in SiGe substrates for PMOS transistor (a) and effective field dependence of hole mobility in biaxial strained Si NMOS (b).

By measuring the piezoresistivity at (100) surface of PMOS channel during uniaxial compression parallel to the channel direction and strain by stretching parallel to the channel width, the hole mobility enhancement has been shown. Fig. 5 shows these complex dependencies of hole mobility on strain for PMOS transistor. It can be seen that, for less strain, compression at $\langle 110 \rangle$ surface increases the hole mobility. Also, for higher strain, the hole mobility is increased by biaxial strain, as by compression, and stretching. It can be concluded that the uniaxial compression at $\langle 110 \rangle$ surface and biaxial stretching are the most effective in terms of increasing the hole

mobility for PMOS transistors.

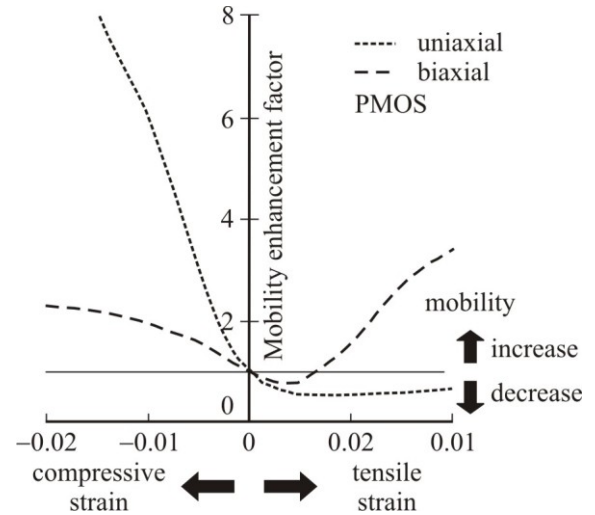


Fig. 5. Hole mobility enhancement factor for PMOS transistor with uniaxial compressive and biaxial tensile strain [23]. The value of E_{eff} is taken to be 1 MVcm^{-1} .

III. MOS STRUCTURES WITH STRAINED LAYERS

The strain is widely accepted as a promising technique which improves CMOS performances through a significant increase of mobility, even from 90 nm CMOS technology. In recent years, substrate and/or process-induced strained channels are successfully integrated in MOS transistors, for the purpose of increasing the channel mobility. Technologically, so far, the biaxially strained layer showed the best results in the case of long channels transistor (over 100% improvement in mobility). However, the contact resistance of the source and drain, saturation velocity, self-heating of relaxation for strained layer complicate the improvement of performances in nano devices.

The advantage of the uniaxial strain access is that it is installed during production of CMOS circuits. However, the scalability and the geometrical dependence are the main problems. The lateral dimensions of the transistors affect the efficiency and strength of strain in the strained layer. It is shown that the process-induced strain layers increase the mobility of both types of carriers and the power drain in NMOS and PMOS transistors. The strain in the channel can be obtained through the individual process steps and the use of strained silicon substrate.

A. Global Strain Technology

The structure of MOS transistor with biaxially strained silicon layer, which has grown on a relaxed SiGe substrate, has been intensively explored in recent years. Also, there have been research on the structures with strained silicon layer on insulator (*Strain-Si On Insulator* - SSOI) [24], where strained/relaxed layers are formed on the buried oxide, and the structures where the strained silicon layer is directly linked to the buried oxide (*Strain-Si Directly On Insulator* - SSDOI) [25]. Common structures and substrates using biaxial strained layers are shown in Fig. 6. The technology for production of

MOS transistor on substrates on which strained layers are formed is called a "Global strain technology".

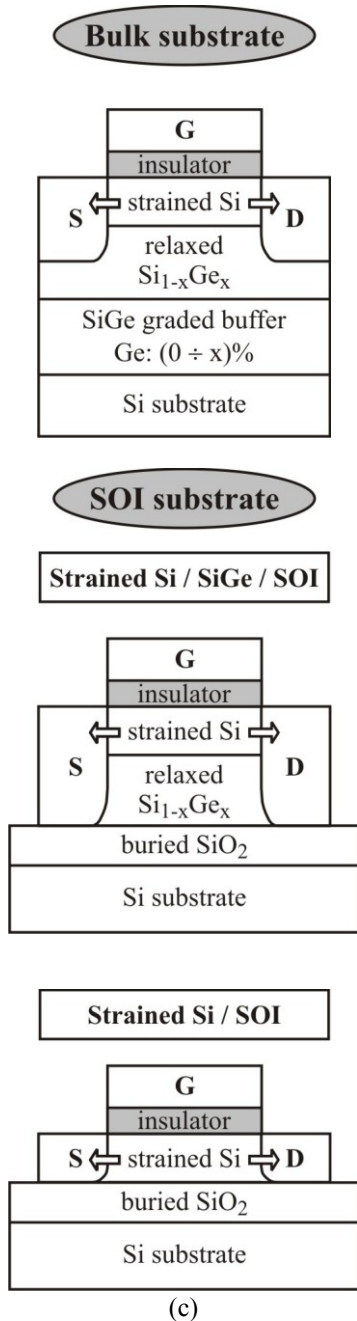


Fig. 6. Cross-sections of typical MOS structures using biaxial strain [3].

As for MOS transistors using silicon substrates from the global strain technology, the research and development of optimized components are implemented on 45 nm and 32 nm CMOS technology. Many research groups have achieved an improvement of current activation in the range of 10-25% with a global strained silicon layer, and gate lengths smaller than 100 nm [25,26]. Also, there has been success in the design of CMOS circuits with gate lengths of 25 nm and the integration of strained silicon layers with gate oxides with high dielectric constant and a metal gate [27].

Main advantages of global strain technology are in obtaining uniformly strained layers with more strength and

possibility of implementing standard CMOS process steps with minimal modifications. On the other hand, there are certain difficulties relating to the limited improvement of PMOS transistor performances with small and medium silicon strain, the occurrence of defects and dislocations at the boundary surfaces, increased production costs and an increase of current leakage at compounds. In transistors with ultra short gate lengths, special attention must be paid to the reduction of the parasitic resistance of the source and drain [3,25].

B. Local Strain Technology

In order to eliminate the limitations of the global strain technology, special attention is paid to the local introduction of structures and materials that will cause strain in the channel of MOS transistors. This process can be conducted in two ways:

- The source and drain of the transistor are formed by epitaxy growth of SiGe composition. These buried SiGe layers, which introduce uniaxial compression in the channel area, are applied in the case of PMOS transistors. Recently it has been shown that NMOS transistor with a layer that is strained by stretching, in which the source and drain formed by selective growth of SiC instead of SiGe, can be implemented (Fig. 7) [28].

- A thin layer of SiN can be applied on the MOS structure, which introduces strain in the channel. In many cases, the SiN layers with stretching are applied for NMOS transistor, while the SiN layers with compression are applied for PMOS transistor (Fig. 7) [29].

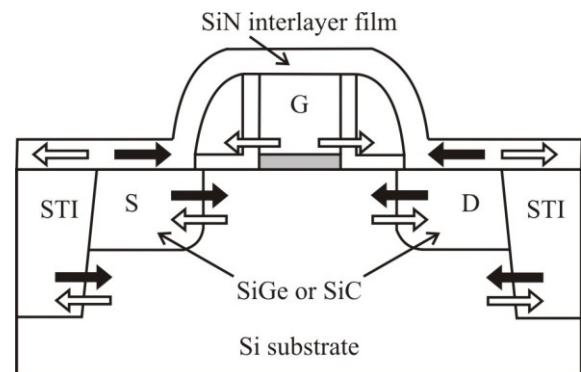


Fig. 7. Illustration of a device structure using different local strain techniques. STI means Shallow Trench Isolation. Black and white arrows indicate compressive and tensile strain, respectively [3].

Beside the above mentioned methods, the strain can be also used for the other parts of the structure, such as, for example, the field insulation, the gate electrode, ... Since the mentioned methods are used in the production of logical LSI circuits for technologies less than 90 nm, the local strain technology has a growing practical importance in CMOS technology [5,30].

The basic advantages of the local strain technology are the possibility of using standard CMOS process with slight modifications and low cost, and acquiring the uniaxial strained PMOS transistors with excellent performance with relatively low strain. However, as in any strain technology, what presents a problem is the process of relaxation of strained layers, which occurs due to the advanced processes in a technological sequence or the component geometry, and a great attention is

devoted to this issue at a moment [3,30].

IV. INFLUENCE OF STRAIN ON ELECTRICAL CHARACTERISTICS

The content of germanium in the SiGe composition used for the source and drain can change the channel compression of 255 MPa to 1.8 GPa, which causes different levels of strain. Fig. 8 shows the output characteristics of PMOS transistor depending on the content of germanium in SiGe S/D pockets. The improvement of drain current with increase of the germanium share is noticeable.

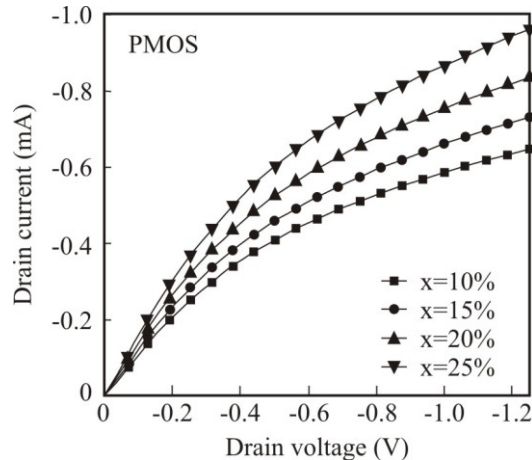


Fig. 8. Drive current enhancement in strained SiGe (S/D) PMOS [31].

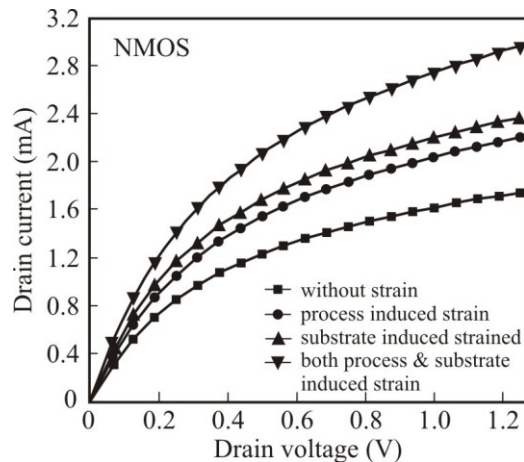


Fig. 9. Drive current enhancement in strained SiGe (S/D) NMOS [31].

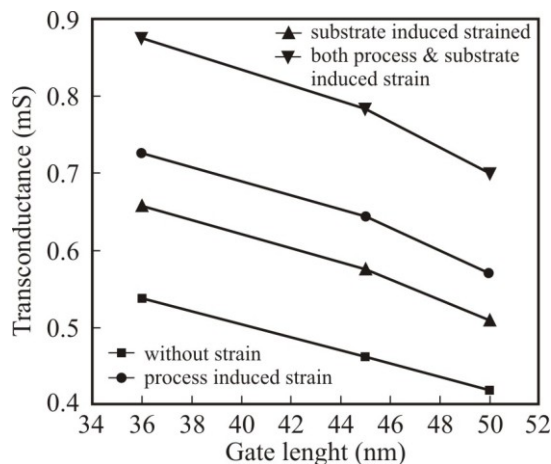


Fig. 10. Transconductance enhancement in strained-Si NMOS [31].

It is particularly interesting to consider the electrical characteristics due to the combined strain, the uniaxial (process-induced) and biaxial (substrate-induced). The combined strain effects for SS NMOS with variable gate lengths (minimum 45 nm) are given in [31], and the performance improvement for more than 62% compared to the conventional NMOS has been shown. Figs 9 and 10 show the combined strain effects on the electrical characteristics of SS MOS.

V. CONCLUSION

Today, modern CMOS technologies cannot be imagined without the strained layers. These layers will, in the future, for the new CMOS technology nodes, have a much more important role, given the limitations of improvements in the standard CMOS technology and the requirements to maintain high current drive. This role imposes the need to develop methods that strain layers can make more compatible with other innovations that are introduced into the standard CMOS process, regardless of whether it is a new material (e.g. for gate of dielectrics), or new structures (i.e. multi-gate structures). Therefore, future research can move in two directions: the optimal design of strained structures and their implementation, on the one hand, and the robustness of the processes and structures to changing performance, with a high level of reliability, on the other hand.

REFERENCES

- [1] <http://www.intel.com/content/www/us/en/silicon-innovations/silicon-innovations-technology.html>
- [2] D. Harame, J. Komfort, J. Kressler, E. Crabbe, J. Sun, B. Meyerson, T. Tice, "Si/SiGe epitaxial-base transistors – Part I: Materials, physics and circuits", *IEEE Transactions on Electron Devices*, vol. 42, pp. 455-468, 1995.
- [3] S Takagi, *Strain-Si CMOS Technology in Advanced Gate Stacks for High-Mobility Semiconductors*, Springer Berlin Heidelberg, 2007, ch. 1.
- [4] D.A. Antoniadis, "MOSFET scalability limits and "new frontier" devices," *2002 Symposium on VLSI Technology, Digest of Technical Papers*, pp. 2-5, June 2002.
- [5] S. Thompson, et al., "A 90 nm logic technology featuring 50 nm strained silicon channel transistors, 7 layers of Cu interconnects, low k ILD, and 1 μm^2 SRAM cell," *2002 International Electron Devices Meeting, IEDM*, pp. 61-64, Dec. 2002
- [6] 2010 Edition of the ITRS, <http://public.itrs.net/>
- [7] C.K. Maiti, N.B. Chakrabarti, S.K. Ray, Strained Silicon Heterostructures: *Materials and Devices*, IEE Circuits, Devices and Systems Series, 12, The Institution of Engineering and Technology, 2001.
- [8] C. K. Maiti, L. K. Berra, S. Chattopadhyay, "Strained-Si heterostructure field effect transistors", *Semiconductor Sci. Technology*, vol. 13, pp. 1225-1246, 1998.
- [9] M. Currie, "Strained silicon: Engineered substrates and device integration", *Proceedings of 2004 International Conference on Integrated Circuit Design and Technology*, pp. 261-268, 2004.
- [10] K. Ismail, M. Arafa, K. L. Saenger, J. O. Chu, B. S. Mererson, "Extremely high electron mobility in Si/SiGe modulation-doped heterostructures", *Applied Physics Letters*, vol. 66, pp. 1077-1079, 1995.
- [11] Z.-Y. Cheng, M. Currie, C. Leitz, G. Taraschi, E. Fitzgerald, J. Hoyt, D. Antoniadis, "Electron mobility enhancement in strained-Si n-MOSFETs fabricated on SiGe-on-insulator (SGOI) substrates", *IEEE Electron Device Letters*, vol. 22, pp. 321-323, 2001.

- [12] S. Dhar, H. Kosina, V. Palankovski, S. Ungersboeck, S. Selberherr, "Electron mobility model for strained-Si devices", *IEEE Transactions on Electron Devices*, vol. 52, pp. 527-533, 2005.
- [13] K. Rim, J. Hoyt, J. Gibbons, "Fabrication and analysis of deep submicron strained-Si N-MOSFET's", *IEEE Transactions on Electron Devices*, vol. 47, pp. 1406-1415, 2000.
- [14] S. Richard, F. Aniel and G. Fishman, "Band diagrams of Si and Ge quantum wells via the 30-band k p method", *Phys. Rev. B*, vol. 72, pp. 245316-7, Dec. 2005.
- [15] S. Takagi, J.L. Hoyt, J.J. Welser, J.F. Gibbons, "Comparative study of phonon-limited mobility of two-dimensional electrons in strained and unstrained Si metal-oxide-semiconductor field-effect transistors", *Journal of Applied Physics*, vol. 80, pp. 1567-1577, 1996.
- [16] M. Rashed, W.-K. Shih, S. Jallepalli, T.J.T. Kwan, C.M. Maziar, "Monte Carlo simulation of electron transport in strained Si/Si_{1-x}Ge_x n-MOSFETs," *1995 International Electron Devices Meeting, IEDM*, pp. 765-768, Dec. 1995.
- [17] T. Mizuno, N. Sugiyama, H. Satake, S. Takagi, "Advanced SOI-MOSFETs with strained-Si channel for high-speed CMOS electron/hole mobility enhancement," *2000 Symposium on VLSI Technology, Digest of Technical Papers*, pp. 210-211, Dec. 2000.
- [18] K. Rim, S. Koester, M. Hargrove, J. Chu, P.M. Mooney, J. Ott, T. Kanarsky, P. Ronsheim, M. Leong, A. Grill, H.-S.P. Wong, "Strained Si NMOSFETs for high performance CMOS technology," *2001 Symposium on VLSI Technology, Digest of Technical Papers*, pp. 59-60, June 2001.
- [19] K. Rim, J. Chu, H. Chen, K.A. Jenkins, T. Kanarsky, K. Lee, A. Mocuta, H. Zhu, R. Roy, J. Newbury, J. Ott, K. Petrarca, P. Mooney, D. Lacey, S. Koester, K. Chan, D. Boyd, M. Leong, H.S. Wong, "Characteristics and device design of sub-100 nm strained Si N- and PMOSFETs," *2002 Symposium on VLSI Technology, Digest of Technical Papers*, pp. 98-99, June 2002.
- [20] S. Takagi, T. Mizuno, T. Tezuka, N. Sugiyama, T. Numata, K. Usuda, Y. Moriyama, S. Nakaharai, J. Koga, A. Tanabe, N. Hirashita, T. Maeda, "Channel structure design, fabrication and carrier transport properties of strained-Si/SiGe-on-insulator (strained-SOI) MOSFETs," *2003. IEDM Electron Devices Meeting*, pp. 3.3.1-4, Dec. 2003.
- [21] R. Oberhuber, G. Zandler, and P. Vogl, "Subband structure and mobility of two-dimensional holes in strained Si/SiGe MOSFET's," *Phys. Rev. B*, vol. 58, pp. 9941-8, Oct. 1998.
- [22] H. Nakatsuji, Y. Kamakura, K. Taniguchi, "A study of subband structure and transport of two-dimensional holes in strained-Si p-MOSFETs using full-band modeling," *2002. IEDM International Electron Devices Meeting*, pp. 727-730, Dec. 2002.
- [23] M. Uchida, Y. Kamakura, and K. Taniguchi, "Performance enhancement of pMOSFETs depending on strain, channel direction, and material," *Proc. Int. Conf. Simul. Semcond. Process Devices*, pp. 315-318, 2005.
- [24] S. Takagi, T. Mizuno, N. Sugiyama, T. Tezuka, A. Kurobe, "Strained-Si-on-Insulator (Strained-SOI) MOSFETs – Concepts, Structures and Device Characteristics," *IEICE transactions on electronics*, vol. 84, pp. 1043-1050, 2001.
- [25] K. Rim, K. Chan, L. Shi, D. Boyd, J. Ott, N. Klymko, F. Cardone, L. Tai, S. Koester, M. Cobb, D. Canaperi, B. To, E. Duch, I. Babich, R. Carruthers, P. Saunders, G. Walker, Y. Zhang, M. Steen, M. Leong, "Fabrication and mobility characteristics of ultra-thin strained Si directly on insulator (SSDOI) MOSFETs," *2003. IEDM International Electron Devices Meeting*, pp. 3.1.1-4, Dec. 2003.
- [26] J.-S. Goo, Q. Xiang, Y. Takamura, H. Wang, J. Pan, F. Arasnia, E.N. Paton, P. Besser, M.V. Sidorov, E. Adem, A. Lochtefeld, G. Braithwaite, M.T. Currie, R. Hammond, M.T. Bulsara, M.-R. Lin, "Band offset induced threshold variation in strained-Si NMOSFETs," *IEEE Electron Device Letters*, vol. 24, pp.568-570, 2003.
- [27] K. Rim, E.P. Gusev, C. D'Emic, T. Kanarsky, H. Chen, J. Chu, J. Ott, K. Chan, D. Boyd, V. Mazzeo, B.-H. Lee, A. Mocuta, J. Welser, S.L. Cohen, M. Leong, H.-S. Wong, "Mobility enhancement in strained Si NMOSFETs with HfO₂ gate dielectrics," *2002 Symposium on VLSI Technology*, pp.12-13, June 2002.
- [28] K.W. Ang, K. J. Chui, V. Bliznetsov, A. Du; N. Balasubramanian, M.-F. Li, G. Samudra, Y.-C. Yeo, "Enhanced performance in 50 nm N-MOSFETs with silicon-carbon source/drain regions," *2004 IEDM IEEE International Electron Devices Meeting*, pp. 1069-71, Dec. 2004.
- [29] H.S. Yang et al., "Dual stress liner for high performance sub-45nm gate length SOI CMOS manufacturing," *2004 IEDM IEEE International Electron Devices Meeting*, pp. 1075-77, Dec. 2004.
- [30] K. J. Kuhn, A. Murthy, R. Kotlyar, and M. Kuhn, "Past, Present and Future: SiGe and CMOS Transistor Scaling", *The Electrochemical Society Transactions*, vol. 33, pp. 3-17, 2010.
- [31] S. S. Mahato, T. K. Maiti, R. Arora, A. R. Saha, S. K. Sarkar and C. K. Maiti, "Strain Engineering for Future CMOS Technologies," *International Conference on Computers and Devices for Communication (CODEC-06)*, 2006.

Study on a Composite Patch Antenna Based on Left Handed Material with Near Zero Index

Jijun Wang, Zhipan Zhu, Yanrong Zhang, Leilei Gong, Yuntuan Fang

Abstract—In this paper, a composite patch antenna based on left handed material (LHM) with near zero index (NZI) is presented. This composite patch antenna is designed by assembling split resonant rings (SRRs) and metal strips on the substrates. This multilayer composite structure results in a metamaterial with NZI near 13.89 GHz. A method of finite difference time domain (FDTD) is used. The results show that the composite antenna's gain improves 0.61 times, and its bandwidth adds 2.95 times compared to the conventional antenna's ones. The results indicate that this composite patch antenna system can reduce return loss of the antenna and increase the gain obviously.

Index Terms—Near zero index, LHM, Photonic crystals, Return loss, Gain.

Original Research Paper
DOI: 10.7251/ELSI1418070W

I. INTRODUCTION

IN the recent years, metamaterials research has received growing attention due to their necessity in developing technologies. Both Left handed material (LHM) and near zero / zero index metamaterials (NZIM / ZIM) have become important, as they are needed for different applications. LHM is an artificially structured material with simultaneously negative permittivity and permeability. As early as 1968, Veselago first analyzed novel physical effects in LHM theoretically [1]. In 2000, the first artificial LHM was fabricated by Smith and his co-workers by combining SRRs and continuous wires [2]. NZIM/ZIM metamaterials are another important branch of metamaterials. According to Snell's law, when the ray is incident from inside the NZIM / ZIM into free space, the angle of refraction will be close to zero, so the refracted rays will be normal to the interface. This property provides a unique method of controlling the direction of emission. In 2002, the group of

Enoch experimentally demonstrated for the first time that energy radiated by a source embedded in a slab of ZIM will be concentrated in a narrow cone in the surrounding media, so a great improvement of directivity was potentially obtained [3], after which many groups have realized NZIM/ZIM metamaterials through experiments [4-5].

The concept of photonic crystals is first introduced by E. Yablonovitch [6] and S. John [7] in 1987. Photonic crystals are a periodic arrangement of dielectric materials. Their internal propagating characteristic of electromagnetic waves in the structure is similar to the propagating of the electrons in semiconductor crystals. If we consider the propagation of an electromagnetic wave in photonic crystals, under certain circumstances a "photonic band gap" can be opened up, and EM waves in the photonic band gap will be forbidden to propagate. Due to this property, the photonic crystals were already used in microwave circuits, antennas [8-9], etc.

In this paper, the FDTD method is employed to analyze a composite patch antenna based on LHM with NZI, and its performance parameters are attained by simulation. The refraction index of the medium is extracted from its S parameters in order to validate the structure. Then, the performance of the composite LHM patch antenna is analyzed by its performance parameters.

II. RESEARCHING METHOD OF THE PATCH ANTENNA

A. FDTD equations

To simulate patch antennas, we use the well-known FDTD method [10-12]. The FDTD method is proving useful in many antenna applications, because it facilitates modelling of complex structures and is capable of characterising antenna performance over a wide-frequency band. Maxwell equations can be transformed into scalar field model by calculating in rectangular coordinate system, and then numerical difference coefficient in the second rank precision is employed to replace differential quotient. The differential equations are made discrete in space-time using the method proposed by Yee, and the patch antenna is made meshed. We assume Δx , Δy are space steps towards x, y direction, respectively, Δt is time step, then we can get difference equations in scalar field model. In transverse electric (TE) mode, Maxwell equations can be transformed into FDTD equations in iteration formulation:

Manuscript received 21 April 2014. Received in revised form 3 July 2014. Accepted for publication 1 October 2014.

Jijun Wang is with Department of Physics, Jiangsu University, Zhenjiang, China (e-mail: 77138169@qq.com).

Zhipan Zhu is with Department of Physics, Jiangsu University, Zhenjiang, China (corresponding author to provide phone: +86 18796022027; fax: +86 511 88791128; e-mail: zhuzhipan888@163.com).

Yanrong Zhang is with Department of Physics, Jiangsu University, Zhenjiang, China.

Leilei Gong is with Department of Physics, Jiangsu University, Zhenjiang, China.

Yuntuan Fang is with School of Computer Science and Telecommunication Engineering, Jiangsu University, Zhenjiang, China.

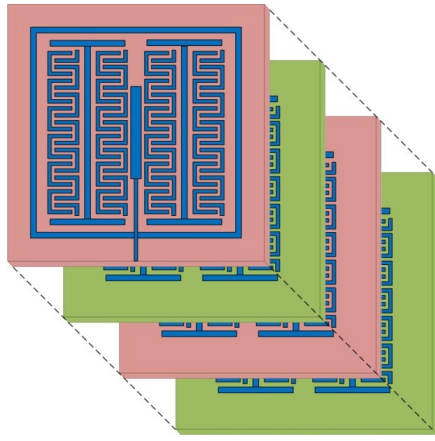


Fig.4. A view of every layer structure combination.

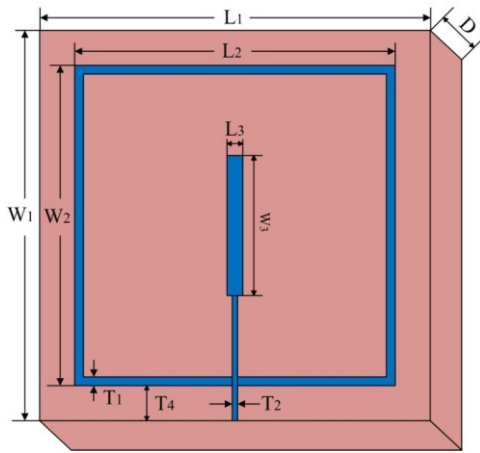


Fig.5. A top view of conventional patch antenna.

III. SIMULATION RESULTS AND ANALYSIS

The above composite patch antenna based on LHM with NZI and conventional patch antenna are analyzed by XFDTD, which is a three-dimensional full wave electromagnetic solver based on the FDTD method. In order to validate the structure, we can use the S parameters, including return loss (or: reflection coefficient) S_{11} and transmission coefficient S_{21} to extract the every layer composite structure's equivalent permittivity ϵ_r and permeability μ_r by Nicolson Ross Weir (NRW) method [14-16]. The extracted results are shown in Fig.6. It can be seen that composite structure's equivalent permittivity ϵ_r and equivalent permeability μ_r are negative near 13.89 GHz. According to ϵ_r , μ_r , the refraction index n is calculated, and it is also negative and near zero, that is n (refraction index of the composite structure) = - 0.12. These results show that the introduction of SRRs and metal straps to the patch antenna may result in negative refractive index with NZI. It indicates that the design of composite structure is feasible.

The property parameters of composite LHM patch antenna are analysed by compared to conventional patch antenna's ones near 13.89 GHz. The corresponding return loss (S_{11}), voltage

standing wave ratio (VSWR) and gain are obtained, which are shown in Fig. 7, Fig.8 and Fig. 9.

The return loss (S_{11}) is shown in Fig. 7, the composite patch antenna based on LHM with NZI has a better return loss, that's -26.14 dB at the frequency of 13.89 GHz. Compared to the conventional patch antenna, the loss is 5.47 dB lower than the conventional one which gets -20.67 dB at 13.88 GHz. The results show that the composite LHM with NZI can improve the antenna's matching condition.

Narrow bandwidth is a major disadvantage of microstrip patch antenna. From Fig. 7, it is found that bandwidth of this composite antenna is 1.26 GHz at 13.89 GHz. 2.95 times is added compared to bandwidth of the conventional antenna 0.32 GHz at 13.88 GHz, showing that the bandwidth of composite patch antenna is enlarged obviously.

In the Fig. 8, this composite antenna's VSWR is 1.1038, which is very close to the ideal condition 1.0. But for the conventional patch antenna, the VSWR is 1.2036, which is much larger than that for the LHM.

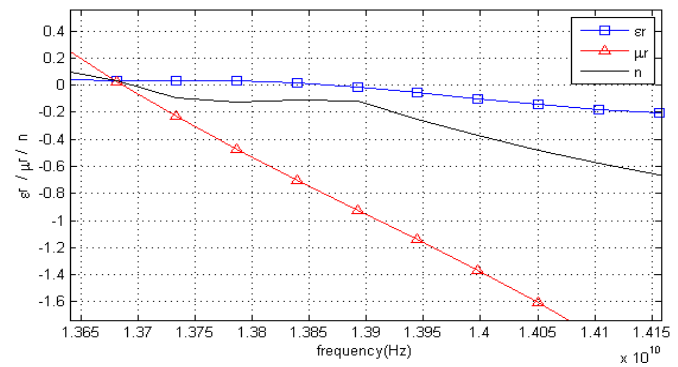


Fig.6. Equivalent permittivity ϵ_r , permeability μ_r and refraction index n of composite patch antenna based on LHM with NZI.

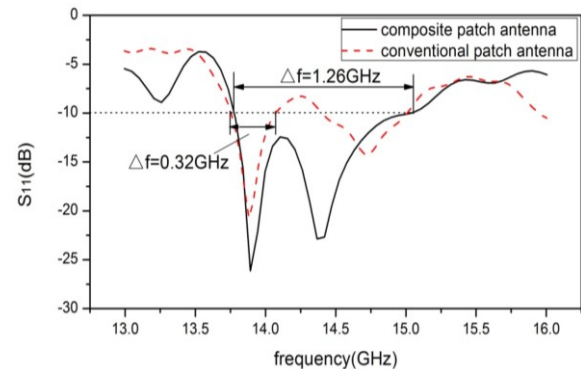


Fig. 7. Return loss (S_{11}) of composite patch antenna based on LHM with NZI and conventional patch antenna.

It can be seen from Fig. 9 that the conventional antenna's maximum gain is 4.301dB at 13.88 GHz, while the composite patch antenna's one is 6.914 dB at 13.89 GHz, which adds 0.61times compared to the conventional antenna's one, and improves 2.613dB. From Fig. 9, it is also found that the directivity of the composite patch antenna based on NZIM is effectively enhanced. The results indicate that the composite LHM with NZI can improve patch antennas' gain obviously. The simulated results are listed in Table 1.

TABLE I
PARAMETERS OF ANTENNAS WITH AND WITHOUT LHM

	Resonant frequency (GHz)	Return loss (dB) ^a	Bandwidth (S ₁₁ =-10dB)	VSWR (voltage standing wave ratio)	Maximum gain (dB)
composite patch antenna	13.89	-26.14	9.1% (1.26GHz/13.89GHz)	1.1038	6.914
conventional patch antenna	13.88	-20.67	2.3% (0.32GHz/13.88GHz)	1.2036	4.301

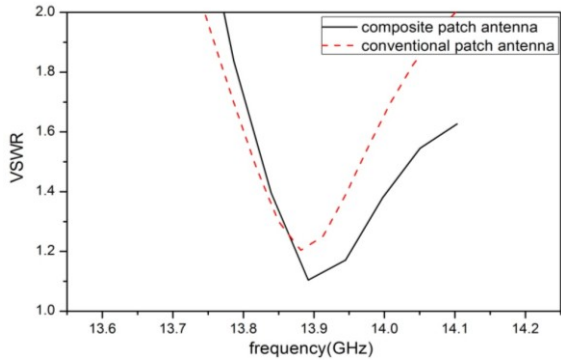


Fig. 8. VSWR of composite patch antenna based on LHM with NZI and conventional patch antenna.

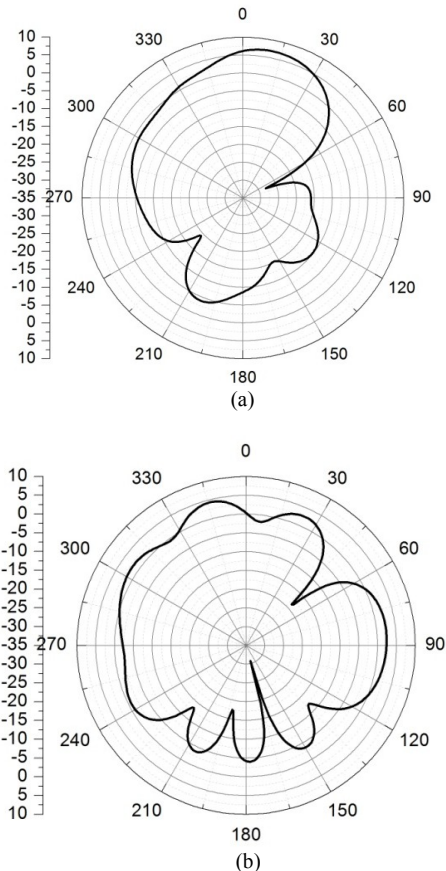


Fig. 9. Gain of: (a) composite patch antenna based on LHM with NZI and (b) conventional patch antenna.

It can be easily found that the composite patch antenna based on LHM with NZI has negative equivalent permittivity ϵ_r and negative equivalent permeability μ_r , and the refraction index n is also negative and near zero in

13.7GHz-14.0GHz, and presents lower return loss and higher gain. This is clear from the following theoretical point of view: the LHM can enhance the EM wave's tunnel effect [14], and the boundary plane between the positive refraction and negative refraction dielectric accord with the surface wave of the EM wave's tunnel traverse model [17]. These surface waves propagate through the boundary plane according to the evanescent waves' coupling effect. The power density near the boundary plane increase rapidly [15], indicating that the equivalent negative refraction structures have the effect of amplifying evanescent waves, so the transmission of surface waves in these models can be enhanced obviously. The refraction index n is negative and near zero. According to Snell's law, when the EM wave is incident from inside the NZIM / ZIM into free space, the angle of refraction will be close to zero, the directivity of the antenna based on NZIM is effectively improved [12]. Such effects can enhance the antenna's gain, and improve the system's matching condition.

What's more, periodically tactic SRRs is introduced based on photonic crystal structure, in the frequency range of the band gap, the spread of electromagnetic waves is hindered in some directions. Such photonic band gap effect could inhibit the surface wave spreading along the basement floor media preferably [8-9]. Therefore, the decrease in absorption of electromagnetic waves and increase in reflection of electromagnetic wave energy lead to reduce return loss of the antenna and increase the gain.

IV. CONCLUSION

A composite patch antenna based on LHM with NZI is designed by assembling SRRs and metal strips on the substrates of conventional antennas. According to our simulation and analysis, we find that this composite patch antenna system can improve patch antenna's property extremely. On the one hand, the electromagnetic wave resonance occurs near $f=13.89$ GHz, and the equivalent permittivity and permeability of composite material are negative, and its refractive index is also negative and near zero. The electromagnetic wave's tunnel effect and evanescent waves' enhancing effect are formed, which can improve the localization extent of electromagnetic wave's energy and enhance the gain apparently. In addition, the directivity of the composite antenna based on NZIM is effectively improved to enhance the antenna's radiation gain. On the other hand, periodically tactic SRRs is introduced based on photonic crystal structure. Such photonic band gap effect could inhibit the surface wave spreading along the substrate

preferably, which will reduce the absorption of electromagnetic wave and increase the reflection of electromagnetic wave energy to the free space. In this case, this composite patch antenna presents lower return loss, higher gain and wider band. Due to these advantages, the use of this composite patch antenna can be extended to mobile communication, satellite communication, aviation, etc.

REFERENCES

- [1] V. G. Vesolago, The electrodynamics of substances with simultaneously negative values of ϵ and μ , *Soznet Physlcs Uspek* 10, 1968, pp.509 – 514.
- [2] D. R. Smith, N. kroll, Negative refraction index in lefthanded materials, *Physical Review Letters* 85, 2000, pp. 2933-2936.
- [3] S. Enoch, G. Tayeb, P. Sabouroux, and P. Vincont, A metamaterial for directive emission, *Phys. Rev. Lett.* 89, 2002, pp. 213902-1–213902-4.
- [4] K. Fang, Y. W. Zhang, F. F. Li, H.T. Jiang, Y.H. Li, W.S. Wang, and H. Chen, Microwave collimation based on zero index metamaterials with Dirac point, *Optics Letters* 37, 2012, pp. 4654-4656.
- [5] G. Lovat, P. Burghignoli, F. Capolino, and D. R. Jackson, Combinations of low / high permittivity and / or permeability substrates for highly directive planar metamaterial antennas, *IET Microw Antennas Propag.*, 1, 2007, pp.177–183.
- [6] E. Yablonovitch, Inhibited spontaneous emission in solid state physics and electronics, *Phys. Rev. Let.* 58, 1987, pp. 2059 -2062.
- [7] S. John, Strong localization of photon in certain disordered dielectric super lattice, *Phys.Rev.Lett.* 58, 1987, pp. 2486 -2489.
- [8] I. Erdinc, S. Kubilay, L. V. John, Miniature printed magnetic photonic crystal antennas embedded into vehicular platforms, *Applied Computational Electromagnetics Society Journal* 26, 2011, pp. 109-114.
- [9] M. Ciobanu, L. Preda, D. Savastru, M. Mihailescu, and M. Tautan, Modeling tunable microwave antenna with photonic crystals. *Journal of Computational and Theoretical Nanoscience* 9, 2012, pp. 778-782.
- [10] S. W. Yang, Y. K. Chen, Z. P. Nie, Simulation of time modulated linear antenna arrays using the FDTD method, *Progress in Electromagnetics Research* 98, 2009, pp. 175-190.
- [11] A. C. M. Austin, M. J. Neve, G. B. Rowe, Modeling propagation in multifloor buildings using the FDTD method, *IEEE Transactions on Antennas and Propagation* 59, 2011, pp. 4239-4246.
- [12] X. T. Dong, X. S. Rao, Y. B. Gan, B. Guo, and W. Y. Yin, Perfectly matched layer absorbing boundary condition for left handed materials, *IEEE Microwave and Wireless Components letters* 14, 2004, pp. 301-303.
- [13] X. H. Song, L. L. Chen, C. H. Wu and Y. N. Yuan, Study on an SRR-shaped left-handed material patch antenna, *Journal of Optics* 13, 2011, pp. 035402-1 – 035402-6.
- [14] Z. M. Zhang, C. J. Fu, Unusual photon tunneling in the presence of a layer with a negative refractive index, *Applied Physics Letters* 80, 2002, pp. 1097 – 1099.
- [15] J. B. Pendry, Negative Refraction Make a Perfect Lens. *Phys. Rev. Lett.* 85, 2000, pp. 3966 - 3966.
- [16] R. W. Ziolkowski, Design, Fabrication, and Testing of Double Negative Metamaterials, *IEEE Trans. Ante. Prop.* 51, 2003, pp. 1516-1528.
- [17] I. V. Shadrivov, A. A. Sukhorukov, Y. S. Kivshar, Nonlinear surface waves in left-handed materials, *Physical Review E* 69, 2004, pp. 016617-1 – 016617-9.

New Blood Level Measurement System in Blood Separating Machine

Miloš Petković, Miroslav Božić, Dragiša Popović, Darko Todorović, and Goran S. Đorđević

Abstract—Standard versions of blood separators typically use medium-price color sensors for a detection of a boundary level between red blood cells and plasma, at the last gate – at hose clamps. Discrete number of sensors is related to a number of significant levels to be detected thus making blood separation potentially faulty and unreliable. Our target was to make flexible, low cost replacement for level detection system that can be easily integrated into the existing product. We came up with an image processing solution that uses USB web-camera, ARM based off-the-shelf board – BeagleBone black and free OpenCV library. Flexibility is held in much higher, selectable number of levels, freely positioned USB camera and brand-free independent processing platform, as well as semi-automatic calibration system. By adding minimum additional electronics, we managed to integrate our solution into existing Blood processing machine. In conclusion, we added a new value to the machine at lower cost in production, increasing measurement frequency and resolution needed for improvement of blood separation process. Next step is to try to use two USB cameras on a custom-made board, for simultaneous level detection on two-channel blood separator, bringing the system integration to the higher level.

Index Terms— Blood separator, red cells / plasma level detection, USB web camera, BeagleBone black.

Original Research Paper
DOI: 10.7251/ELSI1418075P

I. INTRODUCTION

BLOOD separation machines are used for separating red blood cells from plasma. The centrifuged bag of blood is

Manuscript received 20 October 2014. Received in revised form 10 December 2014. Accepted for publication 15 December 2014.

This research and paper were funded by Ministry of science, education and technical development, through project III44004.

M.Sc. Miloš Petković is with the Faculty of Electronic Engineering, University of Nis, 14 Aleksandra Medvedeva, 18000 Nis, Serbia (e-mail: milos.petkovic@elfak.ni.ac.rs).

Miroslav Božić is with the Faculty of Electronic Engineering, University of Nis, 14 Aleksandra Medvedeva, 18000 Nis, Serbia (e-mail: miroslav.bozic@elfak.rs).

Dragiša Popović is with the Faculty of Electronic Engineering, University of Nis, 14 Aleksandra Medvedeva, 18000 Nis, Serbia (e-mail: gile.sherif@gmail.com).

M.Sc. Darko Todorović is with the Faculty of Electronic Engineering, University of Nis, 14 Aleksandra Medvedeva, 18000 Nis, Serbia (e-mail: Darko.Todorovic@elfak.ni.ac.rs).

Prof. Dr. Goran S. Đorđević is with the Faculty of Electronic Engineering, University of Nis, 14 Aleksandra Medvedeva, 18000 Nis, Serbia (e-mail: goran.s.djordjevic@elfak.ni.ac.rs).

inserted into machine where it is being squeezed. The bag content is drained away through two separate tubes, one on the top and one on the bottom of the bag. Red blood cells are settled at the lower half of the bag after centrifuging. When the bag is squeezed they flow through bottom tubing into another bag. Similarly, lighter plasma flows through top tubing into third bag. This method is so called top-bottom and it is common for this type of bags, with top and bottom tube openings. There are other methods for extraction that use different types of bags, with different location of draining tube openings. In order for this particular, top-bottom, method to be efficient it is important to maintain flows through top and bottom tubes equal. Plasma is not only lighter it is more fluent than red blood cells. This means that unregulated draining will cause all of the plasma to leave the bag before the red cells. If this happens, a lot of the remaining content will be trapped. That is why a constant tracking of ratio between those two liquids is needed. When the balance is lost, a clamp stops the flow of less dominating fluid. The more dominant fluid continues to run, eventually returning the balance. When balance is set again, the clamp is opened.

The ratio between plasma and red cells can easily be tracked visually. There is significant difference between them both in transparency and color. A distinctive boundary level can be seen in the centrifuged bag. Blood separators, currently available on the market, typically use medium price color sensors to detect whether red cells reached some level. This means that there must be as many sensors as there are significant levels to detect. Usually, it is eight. The total cost of this solution gets even higher if maintenance is considered. Specifically, additional drawback that comes with these sensors is periodic calibration. Increased number of sensors, due to number of levels, automatically means longer maintenance time, as well. This increases maintenance fees as well as loss of profit during halt in machine usage.

The high price, the need for calibration and somewhat longer maintenance time lead us into search for better solution.

II. IMAGE BASED LEVEL DETECTION METHOD

We browsed the Internet for existing solutions for blood level detection in blood separators. We found no papers written on particular subject. Most blood separator manufacturers are not sharing design details of their products.

Also no particular patents were found on online patent sharing sites. However, we found quite a bundle of papers for liquid level detection in other applications, as well as some commercial sensors. There are several companies that make industrial liquid level measuring sensors, based on optical technologies. Whether they use laser reflection or some other CCD camera method, they are made for industrial purposes and harsh operating conditions. E.g. for casting industry where temperatures rise up to 2000°C, on the contrary, room conditions where blood separators work are quite regulated, due to conventions for good blood preservation. Stated make industrial, off-the-shelf sensors quite expensive and thus in conflict with design goals. Other inconvenience with most of liquid level detection sensors is that they are mostly used for detecting levels in tanks, not small, flexible containers like blood bags. This primarily means that sensor is placed on top of rigid container and use some sort of contactless distance measuring. Without emphasizing any particular solution we will reference following [1-6]. In [1-4] they are using optical methods with camera to measure level in tanks. Although not quite same as what we did, our solution could be described as their mixture, as it uses similar concepts. [5] and [6] are referring to liquid level check in bottles. Although they concentrate on smaller liquid level variation and detection of badly filled bottles they concern with methods that are of interest for our solution. [5] gives quite nice comparison of different image processing methods and their accuracy. However none of the work of others, that we have found, was done for liquids in bags.

The solution that we came up with is image processing based as well. The basic idea is to take video of blood bag, during the separation process, with commercial USB camera, and then do image processing, on some mini PC board, in order to determine boundary level. The camera itself would be placed inside the machine, facing toward already existing small window on the side of machine. The current purpose of this narrow window is to make visual contact between color sensors and the bag. When the sensors are removed there is quite enough space for camera to be placed. Furthermore, body of machine is quite deep, without any parts in the window region. So the camera can be placed far enough from the window to capture it wholly. The decrease in needed distance is also due to wide viewing angles of web cameras. However we used this extra space to leave possibility of slight misalignment between camera focal point and center of the window. So the camera image is set to capture quite an area around the window. This surrounding area appears mostly black, since very little light breaks into machine. This creates quite good contrast between region of interest, which is the window, and the rest of image. After all initial feasibility checkups of the use of a generic web camera gave positive feedback, we went on with image processing algorithm and processing platform selection.

We considered it convenient to use some off the shelf mini PC platform for image processing. Mini PC platforms offer possibility of programming with higher abstraction languages

and easier code portability. They are also available in quite a number in terms of processing power and other features. We chose ARM based board - BeagleBone Black [7]. Primarily cause it was already at our disposal. Another reason is that there is additional plug-in board (cape) with good video camera, particularly for this mini PC. Later performance comparison of this camera cape and a USB camera showed no significant difference. Since latter is much cheaper, but equally suitable, we based rest of the research and the solution on it.

The goal for image processing software was to be as portable as possible. We decided that OpenCV library is therefore a good choice [8, 9]. It is a free library that contains a lot of implemented image processing algorithms, and thus reduces design time. It is highly portable. It offers initial development and testing of image processing algorithm to be done on PC, which is faster than on some mini PC. Latter, only simple code recompiling is needed for it to run on other platforms like Beagle Bone Black (BBB). As source code of library is available, it can be made, with more or less effort, compatible with any platform. However, already compiled shared library versions are available for most known mini PC platforms. Luckily BBB is one of them, which saved us some time. Shared libraries are even installed on official OS. It is Angstrom (Ångström) version of Linux. There are other OS available, like Ubuntu or Android, but we chose to keep using the initial one, which is farcically pre stored on BBB on-board flash memory. We would like to point out that previously mentioned camera cape requires some of processor pins otherwise used for communications with flash memory. Therefore, when camera cape is used, OS should be put on and then loaded from external micro SD card. Although we used official release of Angstrom for SD card, we have noticed, during camera cape testing, that it is less stable than the flashed one. This inconvenience, altogether with already stated in previous paragraph, put us off the camera cape use.

A. Image processing

As mentioned before, our region of interest (ROI) is the narrow vertical window on the bag side of a blood separator. Since both the camera and the window are stationary to each other during machine run, we decided to use static approach to extraction of ROI. In other words, ROI always has the same position in acquired image. So there is no need to constantly run ROI finding algorithms during separation process. This greatly reduces necessary processing power of underlying hardware. Opposed to that, higher number of processed video frames, or lower response time, can be achieved.

Every time blood separator is started ROI coordinates, in terms of image coordinating system, are found. This way we wanted to ensure that possible slight movements of camera do not reduce measurement accuracy. Potential cause of camera twitch could be for example rougher machine handling during transportation. At least, our initial shoddy camera holder was susceptible to this. It was replaced later on with better one, but we kept on startup ROI initialization as security measure.

Anyhow, extraction of ROI coordinates should be fast and solid. Although there is high contrast between window and surrounding, we noticed its fluctuations on window boundaries. As said before, very small amount of light enters the machine. However, above the window there is a strain gauge mass measuring sensor, which aluminum body reflects and scatters light. So, upper side of the window appears pretty irregular. Other sides also shimmer a bit, from time to time. We decided that it is best to add fixed frame with four corner LEDs onto the window. They are solid markers for rectangular ROI determination. This solution is less ambient lighting dependent and thus less error prone. LEDs are the brightest objects on the image and therefore easily extracted, as it can be seen in Fig. 1. If any additional bright enough sources appear, they can be discarded by taking into consideration positional relation of the LEDs to each other. This makes calibration absolutely accurate.

In order to extract the LEDs position from image, the following procedure was used. Camera parameters are firstly set to low exposure and high contrast. Then an image is acquired. In the next step, erode, dilate and blur functions are used to eliminate noise and light dots from grabbed image. This filtering leaves all-black image with four white circles. At the end, we used Hough Circle Transform [10] to detect position of white circles. Unfortunately we had to change this algorithm a bit. The USB web camera, that we used, has some auto white balancing option that we couldn't disable. This means that although very low exposure was set, the camera itself brightens the image, so it looked like in Fig. 1. Note that image is rotated for 90 degrees counterclockwise. The window itself is vertical, but the camera is in portrait position. It was set this way in order to match window elongated height with width of 16:9 resolution camera. During development we rotated image back to vertical position. Later on we left this code out in order to avoid unnecessary loss of time. If image from Fig. 1 were submitted to previously described algorithm, more than 4 white circles would remain in the image. This means that selection of circles would have to follow. We thought that this will increase ROI initialization time and went with different approach. After adjustment of camera parameters, a frame with all LEDs powered off is taken. Then another frame is grabbed after the LEDs are light. Difference between two frames is found, which leaves very few artifacts for removal. After filtering, that is same as in originally planned algorithm; image looks like in Fig. 2. It is further processed with Hough Circle Transform in order to find coordinates of white circle centers. It should be stated that OpenCV functions were used for all mentioned steps like erode, dilate, Hough circle transformation, etc. The last numbered function, returns both center coordinates and diameter of recognized circles. How precise this information is, can be seen in Fig 3. Black dots with coordinates of LED circles were overlaid over image from Fig. 2. It can be noticed that they match the centers of LED circles with quite an accuracy. The rest of white circles are covered with empty, black line, circles to designate recognized sizes of white circles.



Fig. 1 Unprocessed image from camera, LEDs are turned on. Note that image is rotated for 90 degrees, the window is normally vertical. This is due to camera orientation.

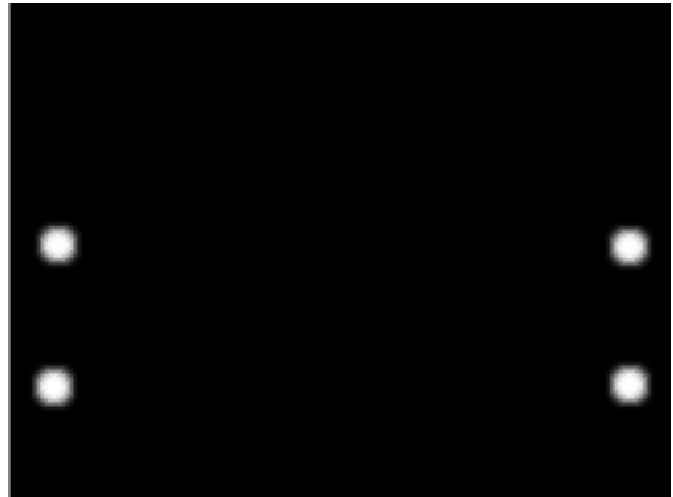


Fig. 2 Image of turned on LEDs, after reference frame subtraction and filtering. Reference frame is taken just before LEDs are light.

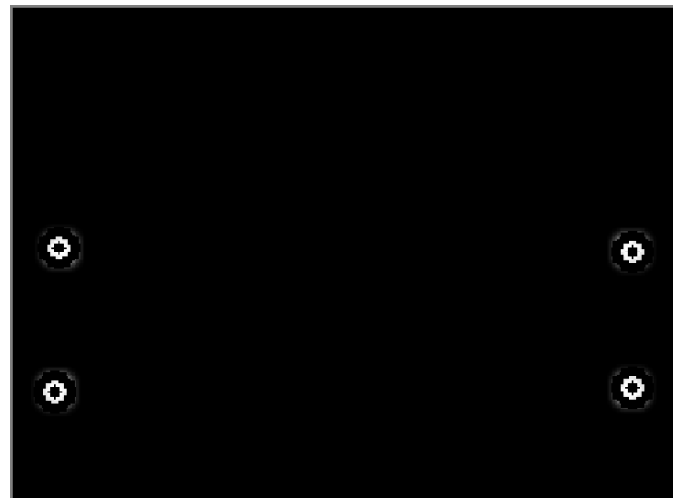


Fig. 3 Found coordinates of LEDs, designated with overlaid black dot in center. The rest of white circles are covered with empty, black line, circles to designate recognized sizes of white circles.

LED circles approximated by the function. This information was used just for the purpose of evaluation of quality of image filtering and precision of OpenCV functions.

After window coordinates are known, other pre-processing transformations can be applied. We used only rectification, as we believed it improves accuracy of the system. Finally, ROI can be extracted for further processing by a boundary level detection algorithm.

ROI is extracted from camera image while settings are close to default ones, typically used with normal ambient light. We lowered brightness only a little. Since center of LEDs are slightly away of the window corners, we have reduced ROI width for arbitrary number of pixels. This doesn't affect measurement accuracy. We don't need all the pixels from the window's width to determine boundary line, as it will be described later in more details.

Image of real ROI can be seen on the right in Fig. 4. Ignore the solid horizontal full and half line, for now, as they were overlaid in post processing. The lower portion is red as transparent red foil was placed over outer side of the window. The upper part is partial view of our laboratory. It is blurred by semitransparent blood bag that was also placed at exterior side of the window. During development, and later on during testing, this setup was used as a replacement for real bag with blood. We considered it as quite a good substitute. It should be noted that this image was acquired on PC. From within the code, a real time stream of ROI was being shown on monitor. This is something that is not possible to achieve only with OpenCV functions on BBB. There seems to be lack of their proper implementation for this platform. The image was saved via snapshot tool from within Windows. It is also pre-rotated in oppose to Fig. 1.-3.

First step in level detection is to find all pixels in ROI that belong to red blood cells part. Since it appear as the reddest part in the image, only single threshold level needs to be determined. All pixels that are red above this level are considered to belong to red blood cells portion. After threshold was experimentally determined, OpenCV function "threshold" was used to extract these pixels. The result is shown on the left in Fig. 4. All pixels that are considered red as red blood cells are shown as white. Others are black. Due to lighting conditions, there can appear some black pixels in white region. We used erode function to remove those rouge black pixels.

Next step is boundary level search itself. It is determined according to the average value of horizontal lines. Rapid change in these average values is a good descriptor of the boundary line. Initially, we calculated average value of entire row. However, we noticed that boundary line was slightly curved at the edges of ROI. Filters and image preprocessing that we used cause curvature. In order to exclude this source of error, we reduce average pixel calculation to middle 60 pixels, thus excluding pixels at window edges. However, later on, results showed that there is no significant increase in accuracy. This ROI reduction also reduces the processing time. Finally, rapid change in these average values is searched

in order to determine exact boundary level location within the window. Again, there is quite distinctive difference in plasma and red cells color.

After boundary level was found for image on the left, it was displayed as overlaid gray line over original ROI image in Fig 4. It could be seen that it is determined with solid accuracy. The thin black line, which appears above gray line, comes from boundary line blurred reflection. In other words, no web camera is able to show edge line with ideal contrast. So edge lines will always appear as blurred transitions from one value to another. So we take middle of the edge as an

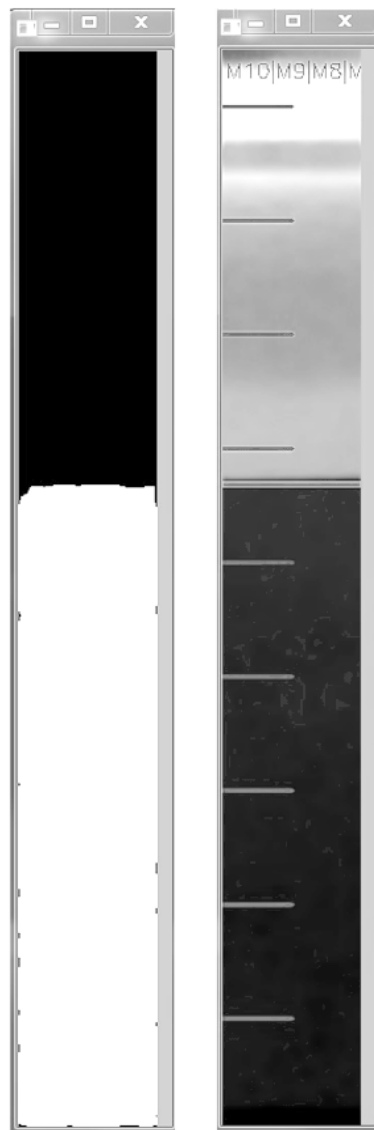


Fig. 4 Level detection on processed image. Left image shows recognized red blood cells portion of bag with white color, and rest of pixels in black. Right image shows real ROI image with designated found boundary line. Horizontal half lines mark the current position of discrete color sensors and gain in accuracy in this method.

actual boundary. The other overlaid half lines designate current position of color sensors. We draw them just to show how big the increase in resolution can be achieved with our method.

We are able to determine boundary level position virtually within accuracy level of about one image line. This is much

higher resolution than with color sensors. However, since our system is to be integrated into existing machines, level conversion is needed. Output from our system is at end with eight significant levels.

B. Software implementation

As previously said, OpenCV library is used for image processing. In particular for fetching camera frames, setting camera parameters, image rotation and rectification, circle (LED) position extraction, inverting image color and detecting blood level. All image-processing code is divided into two functions. One is initialization and calibration function. This function is called once on every machine start up. It accepts as input a *mode* constant. If it is called in service mode then a checking of ROI is performed. In other words, when camera is initially inserted it needs to be faced properly toward window. All four corner diodes must be visible in image. If any of 4 LEDs is not visible due to camera-window misalignment, function will signal this through second argument. In reality, this information is communicated back to camera installer through four LEDs on accompanying board to BBB. Distinctive relation is made between visibility of corner LEDs and displaying LEDs on board. If one corner LED is out of image then corresponding board LED is not shining. When all four board LEDs are turned on then camera is correctly in place and service mode can be exited. When the same function is executed in calibration mode, ROI coordinates are being calculated as previously described. Also, significant middle and other levels are determined, as well as other pre-processing parameters. Separate image processing function takes frame, applies preprocessing like ROI extraction and rectification, and searches for boundary level as mentioned. Function returns detected level.

Other part of software is initialization and communication code. At startup it initialize BBB used peripherals. Altogether, 7 GPIOs and one UART are used. One GPIO is used as input and others as output. Input pin is connected to pull down pushbutton and is used at machine startup to make program run in service mode. If pushbutton is pressed during software initialization phase then service mode is activated. Otherwise it is not checked. So initialization function reads state of input pin only once at beginning. As previously said 4 outputs are used for driving signaling LEDs on accompanying board. The same outputs are used later for signaling level to control part of machine. One output is used to drive latch enable on those 4 outputs. Latch is inserted between BBB and machine control part in order to prevent false code readouts during level change. Last output is used for controlling window LEDs. They are on only during service mode and calibration. Last peripheral, UART, is used for communication with blood separator control unit. A RS232 to RS485 convertor IC is used to interface these two. BBB UART RTS pin is inverted and used as input to IC control pin for direction switching. IC is placed on accompanying board. This board contains all numbered additional electronics. It was designed as plugin board for BBB. If all peripherals are successfully initialized

two main threads are created. Otherwise, error code is displayed on the 4 LEDs. Error codes, as well as status and other important info are being constantly sent to BBB UART 0. It is BBB default stream, and used normally for debugging. We used it for this purpose as well.

The main program basically consists of two threads. One thread is image processing thread. It is infinite loop that calls the image processing function that returns level. The following thread code stores returned value into global level variable and call digital output refresh thread. Digital output refresh thread has short life cycle. It just refreshes state of 4 output pins and dies.

Second main thread is communication thread. It is plain infinite loop that listens for any incoming data from the RS 485 communication conversion IC. When it receives message that is with address of level detection system, it process it and responds. Basically there are two types of message. One is address setup message, and other is level query message. We implemented this according to current machine control unit protocol. Protocol itself allowed us to send 3 bytes of arbitrary data. It was quite sufficient. We used one byte for level, one for system status and third one for error codes.

Whole program was written in C++. Image processing code was developed and tested initially on desktop PC. It was afterwards recompiled and linked with OpenCV libs that were already on BBB Angstrom distribution. We found that these libraries do not support some OpenCV functions, like viewing camera stream in live desktop window. Those functions are primarily important for image processing algorithm development. So, desktop PC was necessary for development of image processing part of code. Rest of program code development was done on desktop PC, but with cross-compiling and remote testing. In other words, code was written in Eclipse IDE with cross-compiler and remote system plugin. When code was compiled it was run directly and debugged remotely on the BBB. Remote debugging did not go that smoothly. It failed from time to time for some reasons.

III. TESTING

System evaluation with real blood has too high price tag for primary testing. It's not just the price of the blood and their somewhat unethical accidental wasting. The blood needs to be kept and handled in a special way. It decays after prolonged exposure to ambient conditions. It would also be needed to re-centrifuge once used blood bag. Due to lack of funding, proper storage and processing machines, we tested our system using red foil placed over bag filled with water. On image, they looked similar enough. At worst case, the system would require only minor reconfiguring before being fully operational. This primarily means setting some new value for the threshold level of the red color detection code.

Test showed that level detection works pretty well even with just room lighting. Nevertheless, we still implemented separate light source control. As far as time is concerned, it takes about 230ms to process small 360p image. For higher

resolution picture, 720p, it even takes 1.2s. The source of long processing time is image rectification. It requires approx. 200ms for 360p image. This was unacceptable and we were forced to remove it. However this only impacts, negatively, cases where camera is highly misaligned with side window. Such circumstances can easily be avoided if fixed camera holders are used, that align window and camera. That way less powerful processing platforms like BBB will suffice.

After rectification removal, processing time was approximately 30ms for 360p frame. For 720p resolution it got up to 70ms. This is still less than 0.1s what was the upper limit set by blood separator manufacturer.

The time itself was measured by comparing BBB system time before call of the image processing function and after it returned detected level. Other part of code took no significant time consumption in overall system cycle.

It is worth noting that processing time could be even faster if direct frame grabbing from camera was done. We had another bad experience with OpenCV and BBB. During initial feasibility check OpenCV was communicating with web camera properly. However after overall code porting and system integration, we suddenly came across their incompatibility. E.g. frames could not be grabbed and some camera settings were inaccessible. Because of that and lack of time we had to perform a quick fix. We managed to set camera properties by executing shell commands, from code, that invoked Linux default driver. In other words, our program calls system program that sends commands to default driver. This can be avoided by using system library for direct communication with default camera driver. This would reduce code flexibility to Linux systems only. However most of mini PC platforms are Linux based anyway. In similar manner we managed camera frame grabbing, too. One possible reason for later inoperability between OpenCV and BBB could be driver update. Also recompiling of the library for BBB could solve the problem. However at the time of testing we had no time to determine the correct cause and the later solution worked.

IV. CONCLUSION

We managed to implement image processing level detection system in blood separation machine. It well surpassed requirements set by blood separators manufacturer. In other words, we accomplished level detection at more than 10 times per second, which is more than enough for the process.

Apart from reducing the system costs, by replacing discrete color sensors, we managed higher detection precision. Near the fairy end of bag squeezing, color of the part with red blood cells tends to lose its strong red color. It becomes somewhat pale. When this happens, color sensors with fix threshold, detects it as plasma instead as red cells. Since process is ended much earlier, approximately 60g of content is left in the bag. Although remaining content is being collected and re-separated, some blood processing companies sees this as great waste. They buy exclusively systems that generate below 30g of remnant. Our solution doesn't necessarily use fix threshold. We believe that, with proper tuning, it can be made to detect

proper boundary level in both cases. In order to accomplish such feats, we would need to get into second, more expensive, phase of testing. This would require use of the real blood.

Another development step is to try to use two USB cameras on a custom-made board, for simultaneous level detection on two channel blood separator. This would bring the system integration to the higher level.

After feedback from manufacturer about our system, we concluded that it would be a really good idea to make a black box shielding. It should guard the conical region between the camera and the window, at least. There are various reasons for this. It would prevent manufacturers to block this empty space with some other inner component, or prevent a loose wire to accidentally do the same. Black non glossy shielding would ensure better image contrast. Currently, contrast is reduced when the machine side is dismantled. Maintenance personnel would like to be able to run the machine in this state during troubleshooting and testing. At present state of our system integration, this would enable ambient light to reflect from various inner components into camera area and possibly cause false reading. At last, integration of our system under one case would make it truly the component for boundary level measuring for blood separating machines.

Finally, we are still determined to improve our algorithm. We removed rectification to achieve shorter processing time, but at the cost of flexibility and self-calibration. It is desirable to keep these two characteristics and we already have a few ideas of achieving them. However, our solution is still quite unique, there are no similar for particular purpose, as far as we know, and it beats currently used design in both performance and price.

REFERENCES

- [1] T. Wang, M. Lu, C. Hsu, C. Chen and J. Tan, "Liquid-level measurement using a single digital camera", *Measurement* 42, Elsevier, 2009, pp. 604-610
- [2] C. Yu, X. Tian, Y. Zhang and Y. Bai, "Liquid Level Measurement by Using an Image Method", in Proc. MACE Third International Conference on Mechanic Automation and Control Engineering, 2012, pp. 1595-1598
- [3] Y. Na, S. Kim, J. Kim and J. Lee, "Development of liquid level control system using web cam", in Conf. 11th International Conference on Control, Automation and Systems (ICCAS), Gyeonggi-do, 2011, pp. 1527-1528
- [4] I. Gil, M. Amparo and M. Pozo, "High resolution simultaneous dual liquid level measurement system with CMOS camera and FPGA hardware processor", Elsevier, *Sensors and actuators A: Physical* 201, pp. 468-476
- [5] K. Pithadiya, C. Modi and J. Chauhan, "Selecting the Most Favourable Edge Detection Technique for Liquid Level Inspection in Bottles", *International Journal of Computer Information Systems and Industrial Management Applications (IJCISIM)*, vol. 3, Mirilabs, 2011, pp. 034-044
- [6] Suntory Limited, "Method and device for detecting average liquid level in a bottle" U.S. Patent 4733095 A, March 22, 1988.
- [7] *BeagleBone Black System Reference Manual, Rev A5.2*
- [8] *OpenCV library*, v 2.4.8
- [9] G. Bradski, A. Kaehler, *Learning OpenCV: Computer Vision with the OpenCV Library*, 1st ed. Sebastapol, CA, USA: O'Reilly Media, Inc., 2008.
- [10] D.H. Ballard, "Generalizing the Hough transform to detect arbitrary shapes", *Pattern Recognition*, vol. 13(2), Elsevier, 1981, pp. 111-122

New Single VDCC-based Explicit Current-Mode SRCO Employing All Grounded Passive Components

Dinesh Prasad, D. R. Bhaskar and Mayank Srivastava

Abstract—This paper proposes a new single resistance controlled sinusoidal oscillator (SRCO) which employs only one voltage differencing current conveyor (VDCC), two grounded resistors and two grounded capacitors. The presented circuit configuration offers the following advantageous features (i) explicit current-mode output with independent control of condition of oscillation (CO) and frequency of oscillation (FO) (ii) low active and passive sensitivities and (iii) a very good frequency stability. The proposed structure can also be configured as (a) trans-admittance low pass filter and band pass filter and (b) quadrature oscillator. The validity of the proposed SRCO, quadrature oscillator and trans-admittance low pass filter and band pass filter has been verified by PSPICE simulations using TSMC CMOS 0.18 μm process model parameters.

Index Terms—VDCC, SRCO, current mode, filter.

Original Research Paper
DOI: 10.7251/ELSI418081P

I. INTRODUCTION

Recently, attention is being given to single active element/active building block (ABB) based SRCOs [1]–[12] and in particular explicit current-mode (CM) SRCOs [13]–[18] and the references cited therein. The use of single ABB has the advantageous features like small chip area, low power dissipation and manufacturing cost as compared to two or more ABBs. The CM operation has received much attention over voltage-mode (VM) operation due to its wider bandwidth and high linearity [19]. The usefulness of explicit CM SRCO is well defined in [20]. The VDCC provides electronically tunable transconductance gain in addition to transferring both current and voltage in its relevant terminals [21]. The application of VDCC as positive/negative lossy/lossless grounded inductance simulation circuits and a floating inductance simulation circuit using single VDCC have been described in [22]–[23]. Therefore, the purpose of this article is to present a new explicit CM SRCO, quadrature oscillator and

trans-admittance low pass filter and band pass filter using single VDCC and with bare minimum passive components. The performance of the various modes both in time-domain and frequency-domain has been verified by PSPICE simulation.

The paper is organized as follows: Proposed circuit is described in section 2. Section 3 includes non ideal analysis and sensitivity performance of the circuit. Frequency stability of the proposed circuit is presented in section 4. Sections 5 and 6 represent the simulation results and conclusion of the paper.

II. PROPOSED CIRCUIT CONFIGURATION

The symbolic notation of recently proposed six-terminals active building block namely, VDCC is shown in Fig. 1, where P and N are input terminals and Z, X, W_P and W_N are output terminals. All terminals of VDCC exhibit high impedance, except the X terminal [22]. The ideal terminal characteristics of VDCC can be defined by the hybrid matrix as given by equation (1). The proposed configuration is shown in Fig. 2

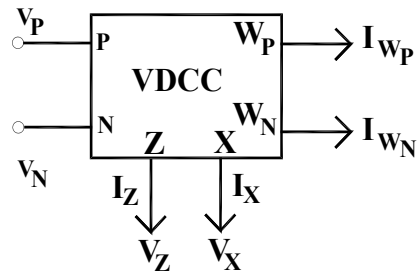


Fig. 1. The symbolic notation of VDCC.

$$\begin{bmatrix} I_N \\ I_P \\ I_Z \\ V_X \\ I_{W_P} \\ I_{W_N} \end{bmatrix} = \begin{bmatrix} 0 & 0 & 0 & 0 \\ 0 & 0 & 0 & 0 \\ g_m & -g_m & 0 & 0 \\ 0 & 0 & 1 & 0 \\ 0 & 0 & 0 & 1 \\ 0 & 0 & 0 & -1 \end{bmatrix} \begin{bmatrix} V_P \\ V_N \\ V_Z \\ I_X \end{bmatrix} \quad (1)$$

Manuscript received 14 August 2014. Received in revised form 19 December 2014. Accepted for publication 25 December 2014.

D. Prasad is with the Faculty of Engineering & Technology, Jamia Millia Islamia, New Delhi, India (phone: +91-11-26981284, e-mail: dprasad@jmi.ac.in)

D. R. Bhaskar is with Faculty of Engineering & Technology, Jamia Millia Islamia, New Delhi, India (e-mail: dbhaskar@jmi.ac.in).

M. Srivastava is with the Amity School of Engineering & Technology, Amity University, Noida, U.P., (e-mail: mayank2780@gmail.com).

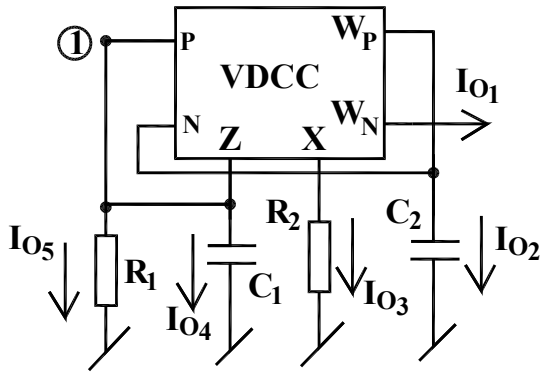


Fig. 2. The proposed circuit topology.

The characteristic equation of the proposed SRCO as shown in Fig. 2, can be derived using routine circuit analysis as:

$$s^2 + s \frac{1}{C_1} \left(\frac{1}{R_1} - g_m \right) + \frac{g_m}{R_2 C_1 C_2} = 0 \quad (2)$$

Thus, from equation (2), it is clear that the CO and FO are obtained as:

$$\left(\frac{1}{R_1} - g_m \right) \leq 0 \quad (3)$$

and

$$\omega_0 = \sqrt{\frac{g_m}{R_2 C_1 C_2}} \quad (4)$$

From equations (3) and (4), CO can be established by R_1 and FO is controlled by R_2 . Hence, both CO and FO are independently controllable.

With the feedback link broken at node '1' and considering the 'P' terminal of VDCC as the input, the two open loop transfer functions realized by the proposed circuit are given by:

$$\frac{I_{o_1}}{V_{in}} = \frac{s \left(\frac{C_2 g_m}{R_2} \right)}{s^2 + s \left(\frac{1}{R_1 C_1} \right) + \frac{g_m}{R_2 C_1 C_2}} \quad (5)$$

$$\frac{I_{o_4}}{V_{in}} = \frac{s^2 g_m}{s^2 + s \left(\frac{1}{R_1 C_1} \right) + \frac{g_m}{R_2 C_1 C_2}} \quad (6)$$

Thus, in this mode, the same configuration can also be used to realize trans-admittance band pass and high pass filters simultaneously. From equations (5) and (6), the natural frequency (ω_0) and bandwidth (BW) are given by

$$\omega_0 = \sqrt{\frac{g_m}{R_2 C_1 C_2}} \quad (7)$$

$$BW = \frac{1}{R_1 C_1} \quad (8)$$

Thus, it is seen that ω_0 and BW are independently tunable.

In the third mode of operation, the various current transfer functions obtained from Fig. 2 are

$$\frac{I_{o_1}(s)}{I_{o_4}(s)} = -\frac{1}{s R_2 C_1} \quad (9)$$

$$\frac{I_{o_2}(s)}{I_{o_4}(s)} = \frac{1}{s R_2 C_1} \quad (10)$$

$$\frac{I_{o_3}(s)}{I_{o_4}(s)} = \frac{1}{s R_2 C_1} \quad (11)$$

$$\frac{I_{o_5}(s)}{I_{o_4}(s)} = \frac{1}{s R_1 C_1} \quad (12)$$

For sinusoidal steady state, Equations (9), (10), (11) and (12) become

$$\frac{I_{o_1}(j\omega)}{I_{o_4}(j\omega)} = \frac{1}{\omega R_2 C_1} e^{j90^\circ} \quad (13)$$

$$\frac{I_{o_2}(j\omega)}{I_{o_4}(j\omega)} = \frac{1}{\omega R_2 C_1} e^{-j90^\circ} \quad (14)$$

$$\frac{I_{o_3}(j\omega)}{I_{o_4}(j\omega)} = \frac{1}{\omega R_2 C_1} e^{-j90^\circ} \quad (15)$$

$$\frac{I_{o_5}(j\omega)}{I_{o_4}(j\omega)} = \frac{1}{\omega R_1 C_1} e^{-j90^\circ} \quad (16)$$

Thus, the phase difference between (I_{o_1} and I_{o_4}) is 90° and between (I_{o_2} and I_{o_4}), (I_{o_3} and I_{o_4}) and (I_{o_5} and I_{o_4}) is -90°

Hence, the currents (I_{o_1} and I_{o_4}), (I_{o_2} and I_{o_4}), (I_{o_3} and I_{o_4}) and (I_{o_5} and I_{o_4}) are in the quadrature form. Thus, in this mode of operation, the circuit works as quadrature oscillator.

III. NON-IDEAL PERFORMANCE AND SENSITIVITY ANALYSIS

Considering the various parasitics of VDCC i.e. the X-terminal impedance consisting of a resistance R_x in series with inductance L_x , the impedance at the W_p -terminal consisting of a resistance R_p in parallel with capacitance C_p , the impedance at the W_n -terminal consisting of a resistance R_n in parallel with capacitance C_n and the impedance at the Z-terminal consisting of a resistance R_z , the FO and CO for the circuit shown in Fig. 2 are given as:

FO:

$$\omega_0 = \sqrt{\frac{\frac{R_x + R_2}{R_p} + \frac{R_x R_1}{R_p R_z} + \frac{R_1 R_2}{R_p R_z} + \frac{R_x R_1 g_m}{R_p} - \frac{R_2 R_1 g_m}{R_p} + g_m R_1}{C_1 C_2 R_1 (R_x + R_2) + C_1 C_p R_1 (R_x + R_2) + C_2 L_x \left(1 + \frac{R_1}{R_z} - R_1 g_m\right) + C_p L_x \left(1 + \frac{R_1}{R_z}\right) + \frac{C_1 L_x R_1}{R_p} - C_p L_x R_1 g_m}} \quad (17)$$

and CO:

$$\left[\begin{array}{c} (R_x + R_2) \left(\frac{C_1 R_1}{R_p} + C_p + \frac{C_p R_1}{R_z} \right) + \\ C_2 (R_x + R_2) (1 - R_1 g_m) + \left\{ C_2 R_1 \left(\frac{R_x + R_2}{R_p} + \frac{R_2}{R_z} \right) + \frac{L_x}{R_p R_z} (R_1 + R_z - R_2 R_1 g_m) - \right. \\ \left. C_p R_1 g_m (R_x + R_2) \right\} \end{array} \right] \quad (18)$$

$$\left[\begin{array}{c} L_x \left\{ R_z (C_1 R_1 + C_2 R_p + C_p R_p) + R_p (C_2 R_1 + C_p R_1) - R_1 R_p R_z (C_2 + C_p) \right\} + \\ C_1 R_1 R_p R_z (R_x + R_2) (C_2 + C_p) \end{array} \right] -$$

$$\left[L_x C_1 R_1 (C_2 + C_p) \left\{ \frac{R_x}{R_p} + \frac{R_2}{R_p} + \frac{R_x R_1}{R_p R_z} + \frac{R_1 R_2}{R_p R_z} + \frac{R_x R_1 g_m}{R_p} - \frac{R_2 R_1 g_m}{R_p} + g_m R_1 \right\} \right] \leq 0$$

The sensitivities of ω_0 with respect to active and passive components are given as:

$$S_{R_1}^{\omega_0} = \frac{\left[\frac{2}{R_p} R_x g_m L_x (C_2 + C_p) + g_m L_x (C_2 + C_p) - \frac{C_1 L_x (R_2 + R_x)}{R_p^2} - \frac{C_1 (R_x + R_2)^2 (C_2 + C_p)}{R_p} \right]}{X} R_1$$

$$S_{R_2}^{\omega_0} = \frac{\left[\left\{ \frac{1}{R_p} + \frac{R_1}{R_p R_z} - \frac{R_1 g_m}{R_p} \right\} Z - \frac{2 C_1 C_2 R_1^2 R_2 g_m}{R_p} - \frac{2 C_1 C_p R_1^2 R_2 g_m}{R_p} - C_1 C_2 R_1^2 g_m - C_1 C_p R_1^2 g_m \right]}{X} R_2$$

$$S_{C_1}^{\omega_0} = - \frac{\left[C_1 R_1 (R_x + R_2) (C_2 + C_p) + \frac{C_1 L_x R_1}{R_p} \right]}{Y}$$

$$S_{C_2}^{\omega_0} = - \frac{\left[C_1 C_2 R_1 (R_x + R_2) + C_2 L_x \left(1 + \frac{R_1}{R_z} - R_1 g_m\right) \right]}{Y}$$

$$S_{R_x}^{\omega_0} = \frac{\left[\left\{ \frac{1}{R_p} + \frac{R_1}{R_p R_z} + \frac{R_1 g_m}{R_p} \right\} Z + \frac{2 C_1 C_2 R_1^2 R_2 g_m}{R_p} + \frac{2 C_1 C_p R_1^2 R_2 g_m}{R_p} - C_1 C_2 R_1^2 g_m - C_1 C_p R_1^2 g_m \right]}{X} R_x$$

$$S_{R_p}^{\omega_0} = \frac{\left[\left\{ C_1 C_2 R_1 (R_x + R_2) + C_1 C_p R_1 (R_x + R_2) + Z \right\} \left\{ - \frac{R_x}{R_p} - \frac{R_2}{R_p} - \frac{R_x R_1}{R_p R_z} - \frac{R_1 R_2}{R_p R_z} - \frac{R_x R_1 g_m}{R_p} + \frac{R_2 R_1 g_m}{R_p} \right\} + \left(\frac{C_1 L_x R_1}{R_p} \right) W \right]}{X}$$

$$S_{R_z}^{\omega_0} = \frac{\left[\left\{ C_1 C_2 R_1 (R_x + R_2) + C_1 C_p R_1 (R_x + R_2) + Z \right\} \left\{ - \frac{R_1 R_2}{R_p R_z} - \frac{R_1 R_x}{R_p R_z} \right\} + \left\{ \frac{C_2 L_x R_1}{R_z} + \frac{C_p L_x R_1}{R_z} \right\} W \right]}{X}$$

$$S_{C_p}^{\omega_0} = -\frac{\left[C_p C_1 R_1 (R_x + R_2) + C_p L_x \left(1 + \frac{R_1}{R_z} \right) - C_p L_x R_1 g_m \right]}{Y}$$

$$S_{g_m}^{\omega_0} = \frac{\left\{ C_1 C_2 R_1 (R_x + R_2) + C_1 C_p R_1 (R_x + R_2) + Z \right\} \left\{ \frac{R_1 R_x}{R_p} - \frac{R_1 R_2}{R_p} + R_1 \right\} + \left\{ C_2 L_x R_1 + C_p L_x R_1 \right\} \left\{ \frac{R_x}{R_p} + \frac{R_2}{R_p} + \frac{R_x R_1}{R_p R_z} + \frac{R_1 R_2}{R_p R_z} + \frac{R_x R_1 g_m}{R_p} - \frac{R_2 R_1 g_m}{R_p} + g_m R_1 \right\}}{X} g_m$$

Where

$$X = 2 \left\{ \left[C_1 C_2 R_1 (R_x + R_2) + C_1 C_p R_1 (R_x + R_2) + C_2 L_x \left(1 + \frac{R_1}{R_z} - R_1 g_m \right) \right] + \left\{ \frac{R_x}{R_p} + \frac{R_2}{R_p} + \frac{R_x R_1}{R_p R_z} + \frac{R_1 R_2}{R_p R_z} + \frac{R_x R_1 g_m}{R_p} - \frac{R_2 R_1 g_m}{R_p} + g_m R_1 \right\} \right\},$$

$$Y = 2 \left[C_1 C_2 R_1 (R_x + R_2) + C_1 C_p R_1 (R_x + R_2) + C_2 L_x \left(1 + \frac{R_1}{R_z} - R_1 g_m \right) + C_p L_x \left(1 + \frac{R_1}{R_z} \right) + \frac{C_1 L_x R_1}{R_p} - C_p L_x R_1 g_m \right],$$

$$Z = \left\{ C_2 L_x \left(1 + \frac{R_1}{R_z} - R_1 g_m \right) + C_p L_x \left(1 + \frac{R_1}{R_z} \right) + \frac{C_1 L_x R_1}{R_p} - C_p L_x R_1 g_m \right\} \text{ and}$$

$$W = \left\{ \frac{R_x}{R_p} + \frac{R_2}{R_p} + \frac{R_x R_1}{R_p R_z} + \frac{R_1 R_2}{R_p R_z} + \frac{R_x R_1 g_m}{R_p} - \frac{R_2 R_1 g_m}{R_p} + g_m R_1 \right\}$$
(19)

Taking $C_1 = C_2 = 0.01\text{nF}$, $C_p = C_n = 0$, $R_z = R_p = R_n = \infty$, $R_x = 0$, $L_x = 0$, $R_1 = 3.675\text{k}\Omega$ and $R_2 = 10\text{k}\Omega$, these sensitivities are found to be $(0, -1/2, 0, 0, 0, -1/2, -1/2, 0, 1/2)$ for equations (19). Thus, all the passive and active sensitivities of natural frequency (ω_0) are low.

IV. FREQUENCY STABILITY

Using the definition of the frequency stability factor S^F as given in [4] $S^F = \left(\frac{d\phi(u)}{du} \right) \Big|_{u=1}$ (where $u = \frac{\omega}{\omega_0}$ is the normalized frequency and $\phi(u)$ represents the phase of the open-loop transfer function of the oscillator circuit), with $C_1 = C_2 = C$, $g_m = \frac{1}{R_1}$ and $g_2 = \frac{1}{R_2} = n g_m$, the S^F of the proposed oscillator is found to be $2\sqrt{n}$. Therefore, very good frequency stability is obtainable by selecting larger value of n .

V. SIMULATION RESULTS

To verify the theoretical analysis, the proposed circuit was simulated using CMOS VDCC [22]. The passive components were selected as $C_1 = C_2 = 0.01\text{nF}$, $R_1 = 3.675\text{k}\Omega$ and $R_2 = 10\text{k}\Omega$. The transconductance of the VDCC is taken as $277.83\mu\text{A/V}$. PSPICE generated output waveforms indicating transient and steady state responses are shown in Fig. 3(a) and 3(b) respectively. These results, thus, confirm the validity of the proposed configuration. Fig. 4 shows the output spectrum, where the frequency of the generated wave is 2.654MHz and the total harmonic distortion (THD) is found to be 1.584% .

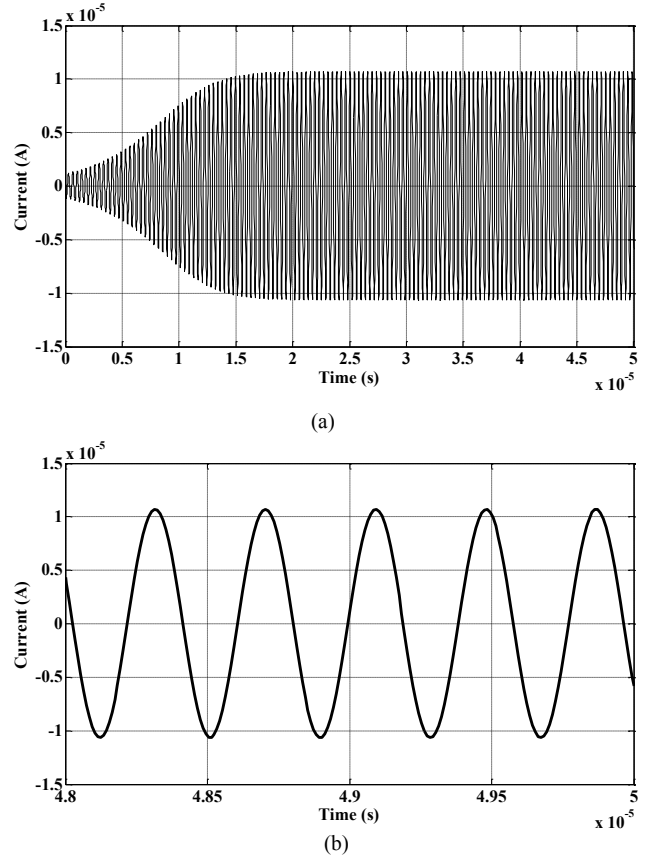


Fig. 3. (a) Transient output waveform, (b) Steady state response of the output.

Fig. 5 shows the frequency response of Transadmittance band pass and high pass filters.

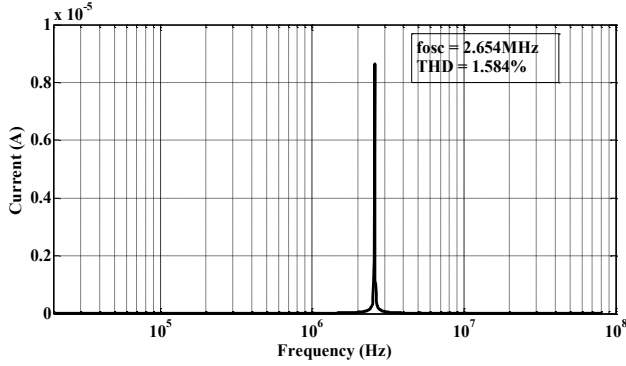


Fig. 4. Simulation result of the output spectrum.

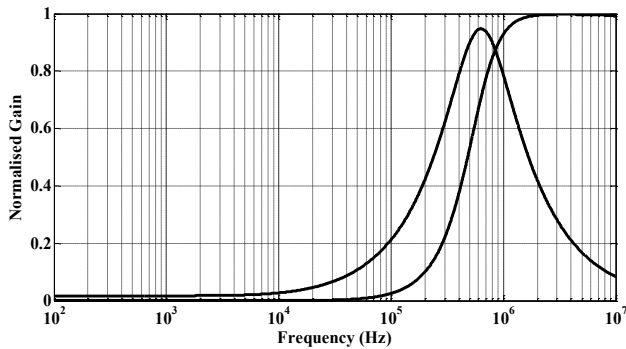


Fig. 5. Frequency response of the simulated filter.

Fig. 6 shows the transient response and steady state response (considering all five currents).

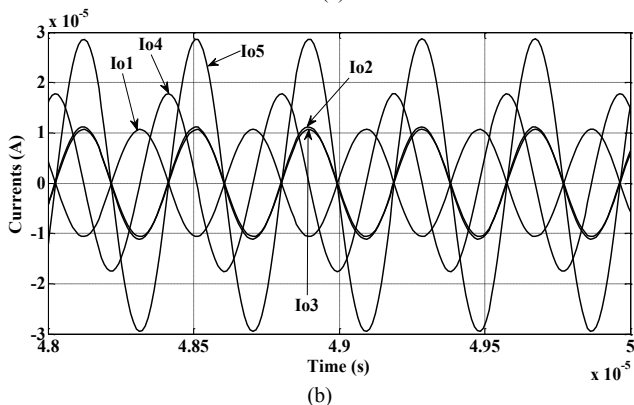
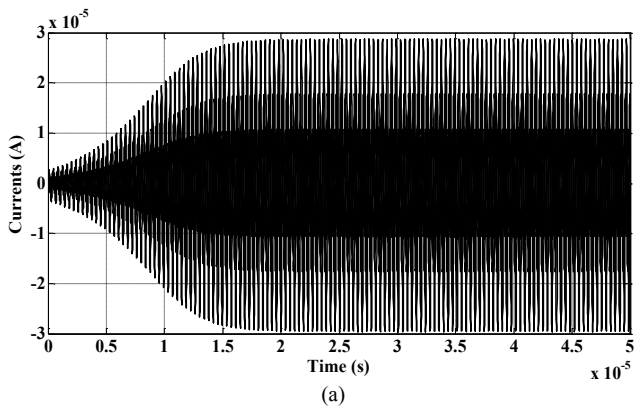


Fig. 6. (a) Transient output waveform, (b) Steady state response of the output.

From Fig. 7 it is clear that the two currents are in quadrature and the measured value of phase shift between two waveforms is $= 89.59^\circ$.

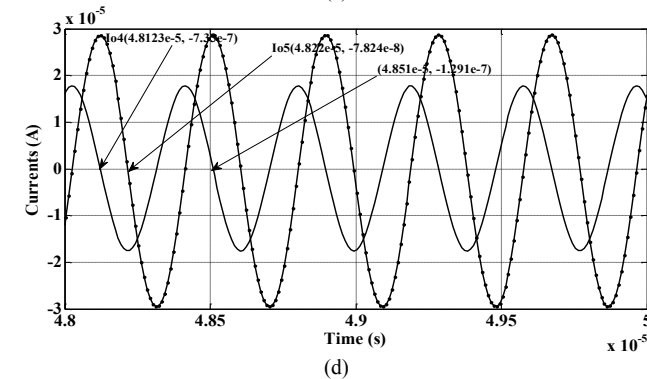
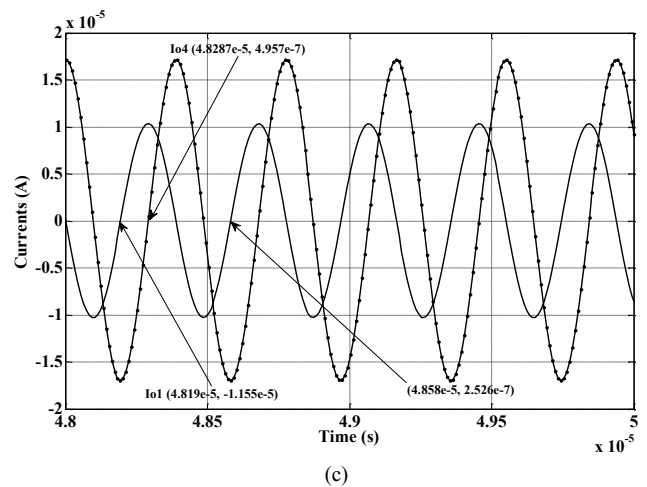
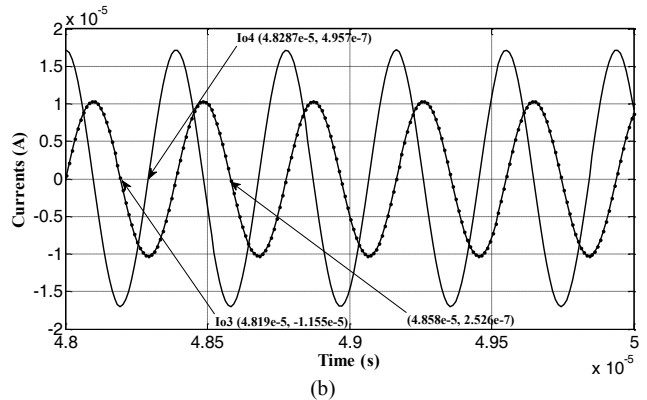
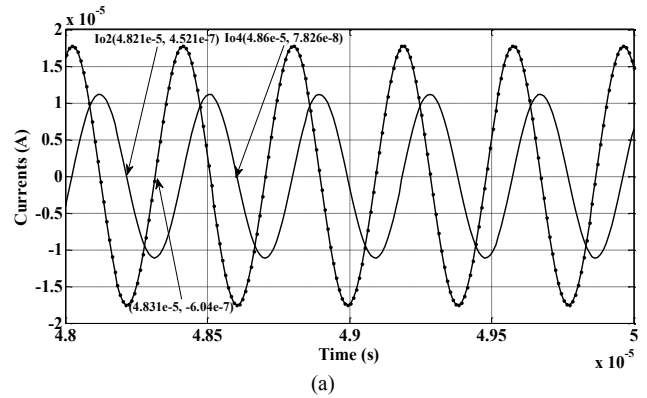


Fig. 7. Currents showing quadrature wave forms.

Fig. 8 shows the transient response of output waveform of Fig. 2 to achieve $S^F = 2$. The circuit of Fig 2 has been checked for robustness using Monte-Carlo simulations, the sample result has been shown in Fig. 9, which confirms that for $\pm 10\%$ variations in the value of R_1 , the value of oscillation frequency remain close to its normal value of 2.654MHz and hence almost unaffected by change in R_1 . The circuit is re- simulated for larger value of n ($n = 100$) and the transient response is shown in Fig. 10. Fig. 11 shows the variation of frequency of output with respect to resistance R_2 . Fig. 12 represents the variation of S^F with n . A comparison with other previously known explicit CM SRCOs using single ABB has been given in Table 1. These results, thus, confirm the validity of the proposed configuration.

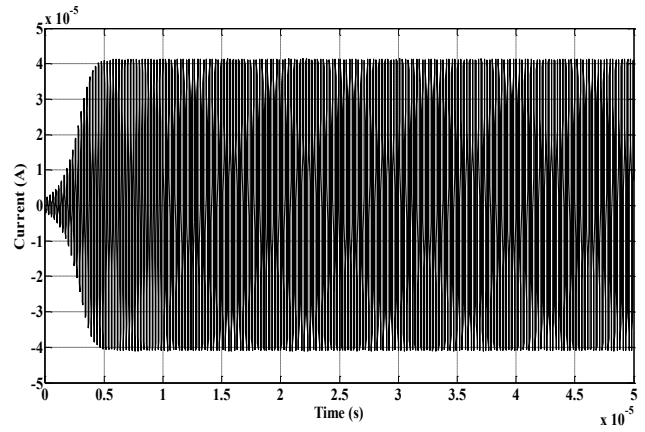


Fig. 8. Transient output waveform for $S^F = 2$.

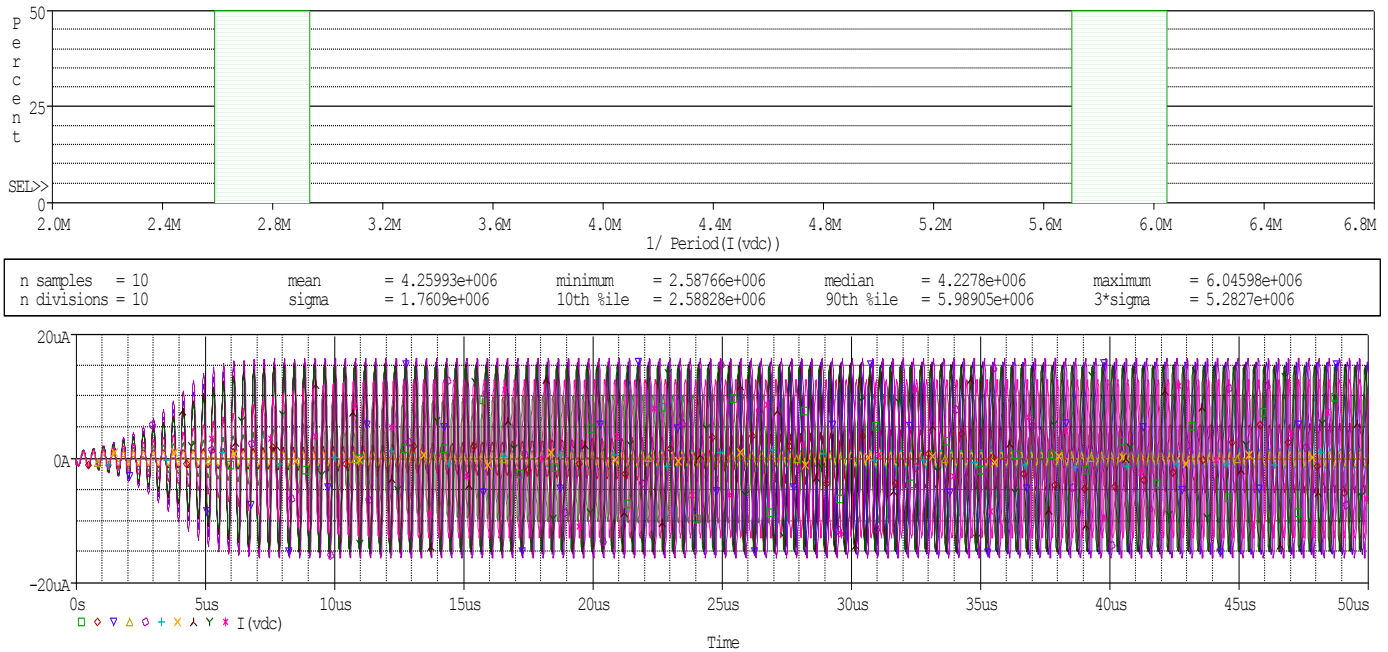


Fig. 9. Result of Monte-Carlo Simulation of oscillator circuit of Fig. 2.

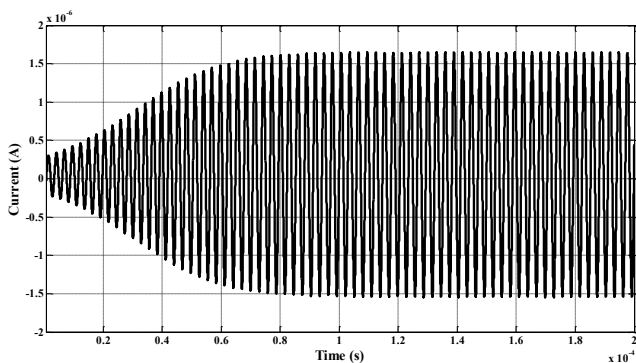


Fig. 10. Transient output waveform for $n = 100$.

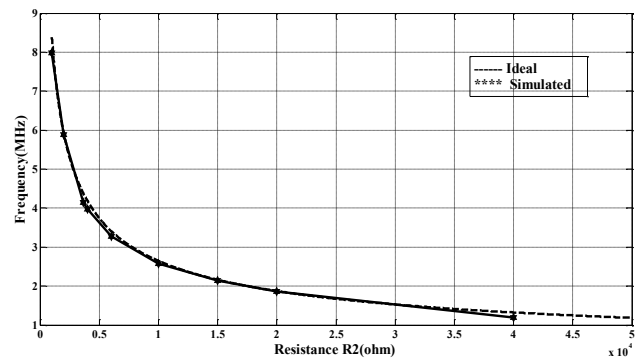
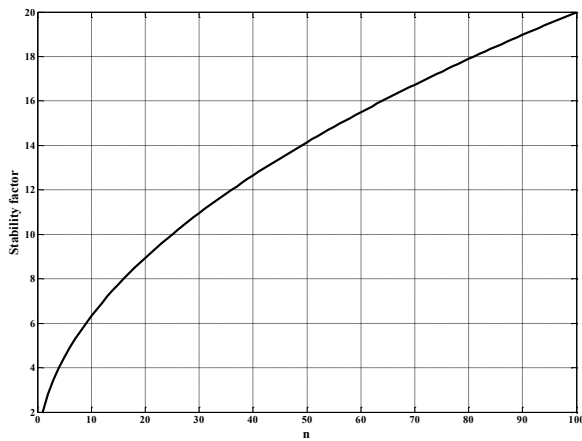


Fig. 11. Variation of frequency with Resistance R_2 .

Fig. 12. Variation of S^F with respect to n .

VI. CONCLUSION

A new SRCO has been proposed using a recently introduced VDCC. The proposed circuit employs four grounded passive components (two grounded resistors and two grounded capacitors) and yet offers independent control of FO through the resistor R_2 and CO through the resistance R_1 , low active and passive sensitivities, realizes two trans-admittance filters (Band Pass and Low Pass) and a very good frequency stability. The performance of the proposed configuration in all three modes has been confirmed by PSPICE simulations.

TABLE 1
COMPARISON OF PROPOSED SRCO WITH OTHER PREVIOUSLY KNOWN SAME TYPE OF SRCOs

Reference	Active Component	Capacitors		Resistors	Availability of Explicit current-mode output/	Independent controllability of CO and FO through grounded resistors	
		Grounded	Floating				
[14]	1 FTFN	Case I					
		3	0	5	YES	NO	
		3	0	5	YES	NO	
		Case II					NO
		1	1	3	YES	NO	
		0	2	4	YES	NO	
		0	2	4	YES	NO	
		1	1	4	YES	NO	
		Case III					NO
		2	1	4	YES	NO	
		1	2	4	YES	NO	
		1	2	4	YES	NO	
		2	1	4	YES	NO	
		Case IV					NO
		1	2	4	YES	NO	
		1	2	4	YES	NO	
1	2	4	YES	NO			
2	1	4	YES	NO			
[15]	1 DVCC	2	0	3	YES	NO	
[16]	1 FDCCII	2	0	3	YES	YES	
[17]	1 CFOA	0	3	3	YES	NO	
		1	2	3	YES	NO	
[18]	1 DVCC	2	0	3	YES	NO	
Proposed	1 VDCC	2	0	2	YES	YES	

REFERENCES

- [1] R. Senani, "New types of sine wave oscillators," *IEEE Trans. on Instrumentation and Measurement (USA)*, vol. 34, no.3, pp. 461-463, Sept. 1985.
- [2] R. Senani and D. R. , Bhaskar, "Single-op-amp Sinusoidal oscillators suitable for generation of very low frequencies," *IEEE Trans. on Instrumentation and Measurement (USA)*, vol. 40, no.4, pp. 777-779, Aug- 1991.
- [3] S. Celma, P. A. Martinez and A. Carlosena, "Minimal realisation for single resistor controlled sinusoidal oscillator using single CCII," *Electron. Letters*, vol. 28, no. 5, pp. 443-444, 1992.
- [4] D. R. Bhaskar and R. Senani, "New Current-Conveyor-based Single-resistance- controlled/ voltage-controlled oscillator employing grounded capacitors," *Electronics Letters*, vol. 29, no. 7, pp. 612-614, 1993.
- [5] C. T. Lee and H. Y. Wang, "Minimum realization for FTFN-based SRCO," *Electronics Letters*, vo. 37, no. 20, pp. 1207-1208, 2001.
- [6] D. R. Bhaskar, "Grounded -capacitor SRCO using only one PFTFN," *Electronics Letters*, vol. 38, no. 20, pp. 1156-1157, 2002.
- [7] J. J. Chen, C. C. Chen, H. W. Tsao and S. I. Liu, "Current-mode oscillator using single current follower," *Electronics Letters*, vol. 27, no.22, pp. 2056-2059, Oct. 1991.
- [8] S. Ozcan, A. Toker, C. Acar, H. Kuntman and O. Cicekoglu, "Single resistance-controlled sinusoidal oscillators employing current

- differencing buffered amplifier,” *Microelectronics Journal*, vol. 31, pp. 169-174, 2000.
- [9] U. Cam, “A Novel Single-Resistance-Controlled Sinusoidal Oscillator Employing Single Operational Transresistance Amplifier,” *Analog Integrated Circuits and Signal Processing*, vol. 32, pp. 183-186, 2002.
- [10] V. K. Singh, R. K. Sharma, A. K. Singh, D. R. Bhaskar and R. Senani, “Two new canonic single-CFOA oscillators with single resistor controls,” *IEEE Trans. on Circuits and Systems II: Express Brief (USA)*, vol. 52, no. 12, pp. 860-864, 2005.
- [11] U. Cam, A. Toker, O. Cicekoglu and H. Kuntman, “Current-mode high output impedance sinusoidal oscillator configuration employing single FTFN,” *Analog Integr. Circ. and Sig. Process.*, vol. 24, pp. 231-238, 2000.
- [12] D. Prasad, D. R. Bhaskar and A. K. Singh, “Realisation of single-resistance-controlled sinusoidal oscillator: A new application of the CDTA,” *WSEAS Trans. Electron.*, vol. 6, no. 5, pp. 257-259, 2008.
- [13] M. T. Abuelmatti, “Grounded-capacitor current-mode oscillator using single current follower,” *IEEE Trans. on Circuits and Systems I: Funda. Theor. And app.*, vol. 39, no. 12, pp. 1018-1020, Dec. 1992.
- [14] M. T. Abuelmatti and H. A. Al-Zaher, “Current-mode sinusoidal oscillator using single FTFN,” *IEEE Trans. on Circuits and Systems II: Anal. and Dig. Sig. Process.*, vol. 46, no. 1, pp. 69-74, Jan. 1999.
- [15] S. S. Gupta and R. Senani, “Grounded-capacitor current-mode SRCO: Novel application of DVCCC,” *Electronics Letters*, vol. 36, no. 3, pp. 195-196, Feb. 2000.
- [16] C. M. Chang, B. M. Ai-Hashimi, H. P. Chen, S. H. Tu and J. A. Wan, “Current-mode single resistance controlled oscillators using only grounded passive components” *Electronics Letters*, vol. 38, no. 19, pp. 1071-1072, 2002.
- [17] R. Senani and R. K. Sharma, “Explicit-current-output sinusoidal oscillators employing only a single current-feedback op-amp” *IEICE Electron. Express*, vol. 2, no. 1, pp. 14-18, 2005.
- [18] V. Aggarawal, S. Kilinc and U. Cam, “Minimum component SRCO and VFO using a single DVCCC,” *Analog Integrated Circuits and Signal Processing*, vol. 49, no. 2, pp. 181-185, 2006.
- [19] C. Toumazou, F. J. Lidgley and D. G. Haig, “Analogue IC Design: The current-mode approach” London: Peter Peregrinus Limited, 1990.
- [20] D. R. Bhaskar and R. Senani, “New FTFN-based grounded capacitor SRCO with explicit current-mode output and reduced number of resistors,” *AEU: Int. J. Electron. Commun.*, vol. 59, pp. 48-51, 2005.
- [21] D. Bielek, R. Senani, V. Biolkova and Z. Kolka, “Active elements for analog signal processing; classification, review and new proposals,” *Radioengineering*, vol. 17, no. 4, pp. 15-32, Dec. 2008.
- [22] F. Kacar, A. Yesil, S. Minaei and H. Kuntman, “Positive/ negative lossy/ lossless grounded inductance simulators employing single VDCC and only two passive elements,” *AEU, Int. J. of Electron. and Comm.*, vol. 68, no. 1, pp. 73-78, Jan. 2014.
- [23] D. Prasad and J. Ahmad, “New Electronically-Controllable Lossless Synthetic Floating Inductance Circuit Using Single VDCC” *Circuits and Systems*, vol. 5, no. 1, pp. 13-17, Jan. 2014

Amplitude Malformation in the IFFT Ocean Wave Rendering under the Influence of the Fourier Coefficient

Lining Chen, Yicheng Jin, and Yong Yin

Abstract—Although Tessendorf’s IFFT Gerstner wave model has been widely used, the value of A , a constant of the Fourier coefficient, is not given. A will strongly influence the shape of the rendered ocean wave and even cause amplitude malformation. We study the algorithm of the IFFT Gerstner wave, and give the method of A calculating. The method of the paper can guarantee there is no amplitude malformation in rendered ocean waves. The expression of the IFFT Gerstner wave with the amplitude of the cosine wave is derived again. The definite integral of the wave number spectrum is discretized. Further, another expression of the IFFT Gerstner wave is gotten. The Fourier coefficient of the expression contains the wave number spectrum and the area of the discrete integral domain. The method makes the shape of the generated wave stable. Comparing Tessendorf’s method with the method of the paper, we find that the expression of A should contain the area of the discrete integral domain and the spectral constant of the wave number spectrum. If A contains only the spectral constant, the amplitude malformation may occur. By reading some well known open source codes, we find that the code authors adopted some factitious methods to suppress the malformed amplitude. Obviously, the code authors have already noticed the phenomenon of the malformation, but not probed the cause. The rendering results of the codes are close to that of the method of the paper. Furthermore, the wave potential is computed using the Gerstner wave model directly, the author find it is quite close to that of the paper. The experimental results and comparisons show that the method of the paper correctly computes the wave potential and effectively solves the problem of amplitude malformation.

Index Terms—Gerstner wave, IFFT, ocean wave spectrum, Riemann sum.

Original Research Paper
DOI: 10.7251/ELS1418089C

Manuscript received 16 August 2014. Received in revised form 18 December 2014. Accepted for publication 25 December 2014. This work was supported by National High-Tech Research and Development Program of China (863 Program) (No. SS2015AA010504).

Lining Chen is with the Laboratory of Marine Dynamic Simulation & Control, Dalian Maritime University, Dalian, China 116023 (phone: 0086-15998558716, e-mail: chenlining19811011@hotmail.com)

Yicheng Jin is with the Laboratory of Marine Dynamic Simulation & Control, Dalian Maritime University, Dalian, China 116023 (phone: 0086-041184727197, e-mail: jycdmu@dlnu.edu.cn)

Yong Yin is with the Laboratory of Marine Dynamic Simulation & Control, Dalian Maritime University, Dalian, China 116023 (phone: 0086-041184729651, e-mail: bushyinu_dmu@263.net)

I. INTRODUCTION

THE reproduction of the ocean wave is an important and challenging research topic in computer graphics. Many fields of activity rely on it: virtual reality, movies, games, maritime simulators and so on.

Bruce [1] and Nelson [2] linearly summed cosine waves to reproduce the height field of the sea surface. The rendered ocean wave is linear and regular. However, the real ocean wave is nonlinear and irregular [3]. To get more realistic results, researchers began to employ nonlinear methods. The Gerstner wave is an exact nonlinear solution for waves of finite amplitude on deep water [4], and is widely applied in ocean wave simulation. Fourier et al [5] introduced the Gerstner wave to ocean wave rendering, and added the random phase shift in the model. So the rendered wave is irregular as well as nonlinear. Thon et al [6] and Fréchet [7] applied the directional spectrum in the Gerstner wave model. The directional spectrum is gotten through observation, so the works of [6, 7] combined the observational oceanographic data with the Gerstner wave model. Consequently, the approaches of [6, 7] are also named as “hybrid approaches” [8]. The geometry of the sea surface can be optimized by some approaches, such as the adaptive surface mesh [9], the quad tree [10], the real-time adapting mesh [11], and the fractal reconciliation [12]. The Perlin noise [6, 13] was added to the height field as random disturbance. Additionally, Prachumrak et al [14] realized the interaction between the floating object and the sea surface.

The direct usage of the Gerstner wave, as mentioned above, is very convenient. However, if a lot of cosine waves are involved, the summation becomes expensive. A cheaper alternative exists by way of IFFT [15], i.e. the IFFT Gerstner wave. IFFT has a large degree of parallelism in each stage of the computation [16] and its implementation is efficiently speeded up by GPU [17]. Tessendorf [18] is the pioneer of applying the IFFT Gerstner wave model in graphics. The Fourier coefficient of Tessendorf’s method contains the wave number spectrum and random numbers, so the generated wave is irregular and nonlinear. The optimizing approach for the geometry included the concentric circle grid [19] and clipmap [20]. By the optimization, the mesh of the geometry is refined or coarsened according to the eye position. Mitchell [21] and Miandji et al [22] utilized image processing algorithms to increase the resolution of the sampled height map.

Swierkowski et al [23] generated the ship wave on the IFFT sea surface. Weerasinghe et al [24] combined the IFFT Gerstner wave with 6-DOF (degree of freedom) ship motion model. The Perlin noise [25], and the high frequency data [26] can also add to the IFFT sea surface. What is more, the model of the IFFT Gerstner wave was also used to create the special effects, such as splashing [27, 28], the whitecap [29] and the foam [30].

To facilitate reading, some parameters and symbols are defined here. We use Ψ to denote the wave number spectrum, and A_Ψ the spectral constant of the corresponding wave number spectrum. $A_{\Psi,Ph}$ is the spectral constant of the Phillips spectrum, $A_{\Psi,PM}$ is that of Ψ_{PM} in expression (32), and $A_{\Psi,J}$ is that of Ψ_J in expression (33). A represents the numeric constant of the Phillips spectrum in expression (4).

The IFFT Gerstner wave was raised in [18], and [19-30] directly made use of it. All of them achieved satisfactory results. A is a numeric constant of the Phillips spectrum which is included in the expression of the Fourier coefficient, so A is also contained in the expression of the Fourier coefficient. Although Tessendorf's method has been widely used and studied, the author finds the value of A is not given in [18-30]. However, A strongly influences the shape of the generated ocean wave. If the expression of A contains only $A_{\Psi,Ph}$, the amplitude malformation may occur. The larger the area of the sea surface, the more serious the amplitude malformation. So the author thinks that the method of A calculating should be considered and provided.

The paper studies the model of the IFFT Gerstner wave, and gives the method of A calculating. The expression of the IFFT Gerstner wave with the amplitude of the cosine wave is derived again. To begin with, we discretize the definite integral of the wave number spectrum with the right Riemann sum. The area of the discrete integral domain depends on the sample mode for the wave number vector. Further, we can get an expression of the IFFT Gerstner wave. The Fourier coefficient of the expression contains the wave number spectrum and the area of the discrete integral domain of the sampled wave number vector. Comparison shows that the expression of A should include the spectral constant of the wave number spectrum as well as the discrete integral domain. Till now, a confusing problem is brought. Since A is not given, how did [18-30] get good rendering results? The author infers that some factitious methods may be taken to treat the amplitude malformation. The first method is setting A very small. Although [18-30] shared the same method and wave number spectrum, i.e. the Phillips spectrum, A , the numeric constant of the spectrum, is not given. So the user of the method in [18] can set A very small to treat the amplitude malformation. The second method is to multiply the height field by a small factor. After reading three widely used open source codes, osgOcean [31], oceanFFT [32] and fftrefraction [33], the author finds that the code authors adopt the factitious methods. This confirms the author's inference. The factitious method is effective but lack of basis. When compute the wave potential of the method of directly

using the Gerstner wave model, we find the computed wave potential is close to that of the method of the paper. The comparisons and experiments results prove that the method of the paper correctly computes the wave potential, and effectively solves the problem of amplitude malformation.

II. PROBLEM STATEMENT

The model of the IFFT Gerstner wave [18] is expressed as:

$$\begin{cases} h(\vec{x}_{pq}, t) = \sum_{\vec{k}_{ij}} \tilde{h}(\vec{k}_{ij}, t) \exp(\sqrt{-1}\vec{k}_{ij} \cdot \vec{x}_{pq}), \\ \mathbf{D}(\vec{x}_{pq}, t) = \sum_{\vec{k}_{ij}} -\frac{\vec{k}_{ij}}{k} \tilde{h}(\vec{k}_{ij}, t) \exp(\sqrt{-1}\vec{k}_{ij} \cdot \vec{x}_{pq}). \end{cases} \quad (1)$$

where h is the elevation of the sea surface,

\vec{x}_{pq} is the horizontal position, $\vec{x}_{pq} = (x_p, y_q) = (Lp/n, Lq/n)$,

t is the time,

\tilde{h} is the Fourier coefficient,

\vec{k}_{ij} is the wave number vector, $\vec{k}_{ij} = (k_{x,i}, k_{y,j}) = (2\pi i/L, 2\pi j/L)$, and $k = \|\vec{k}_{ij}\|$,

L is the width of the rendered ocean wave surface,

p, q, i and j are integers, and $-n/2 \leq p, q, i, j < n/2$,

n is a positive integer, $n = 2^m$, and m is a positive integer,

$\sqrt{-1}$ is the imaginary unit, i.e. $(\sqrt{-1})^2 = -1$,

\mathbf{D} is the choppy wave vector.

So the 3D coordinate of a point on the sea surface is $(\vec{x}_{pq} + \lambda \mathbf{D}(\vec{x}_{pq}, t), h(\vec{x}_{pq}, t))$. \tilde{h} is expressed as:

$$\begin{aligned} \tilde{h}(\vec{k}_{ij}, t) &= \tilde{h}_0(\vec{k}_{ij}) \exp(\sqrt{-1}\omega_k t) \\ &+ \tilde{h}_0^*(-\vec{k}_{ij}) \exp(-\sqrt{-1}\omega_k t). \end{aligned} \quad (2)$$

where $*$ is the notation for the complex conjugate, ω_k is the circular frequency, and \tilde{h}_0 is expressed as:

$$\tilde{h}_0(\vec{k}_{ij}) = \frac{1}{\sqrt{2}} (\varepsilon_1 + \sqrt{-1}\varepsilon_2) \sqrt{\Psi_{Ph}(\vec{k}_{ij})}. \quad (3)$$

where ε_1 and ε_2 are independent Gaussian random numbers.

E and Var denote the expectation and variance respectively. $E(\varepsilon_1) = E(\varepsilon_2) = 0$, and $\text{Var}(\varepsilon_1) = \text{Var}(\varepsilon_2) = 1$. And Ψ_{Ph} is the Phillips spectrum, expressed as:

$$\Psi_{Ph}(\vec{k}) = A \frac{1}{k^4} \exp\left(-\frac{g^2}{U^4 k^2}\right) \cos^2(\theta - \alpha). \quad (4)$$

where A is a numeric constant, U is the wind velocity, and α is the angle between the wind direction and x axis.

$\Psi_{Ph}(\vec{k})$ is in the spectral form raised in [34], i.e.

$\Psi_{ph}(\vec{k}) \propto k^{-4} f(\theta)$. But neither [34] nor [18-30] worked out the value of A . The author analyzed the structure of $\Psi_{ph}(\vec{k})$, and found its frequency spectrum is similar to the P-M spectrum in form. If the Phillips and P-M spectra share the same wave potential, $A_{\Psi,ph} = 3.48 \times 10^{-3}$, and U should be the wind velocity at the height of 19.5 m above the sea surface, i.e. $U_{19.5}$ [35]. Yet when the author applies $A = A_{\Psi,ph}$ in rendering, the shape of the generated ocean wave is not stable. Figure 1 demonstrates the rendering results. The amplitudes of the waves in both Figure 1(a) and (b) are overlarge, and the bigger the width L is, the more serious the malformation is. So the author thinks that the method in [18] need re-examined, and the method of A calculating should be provided.

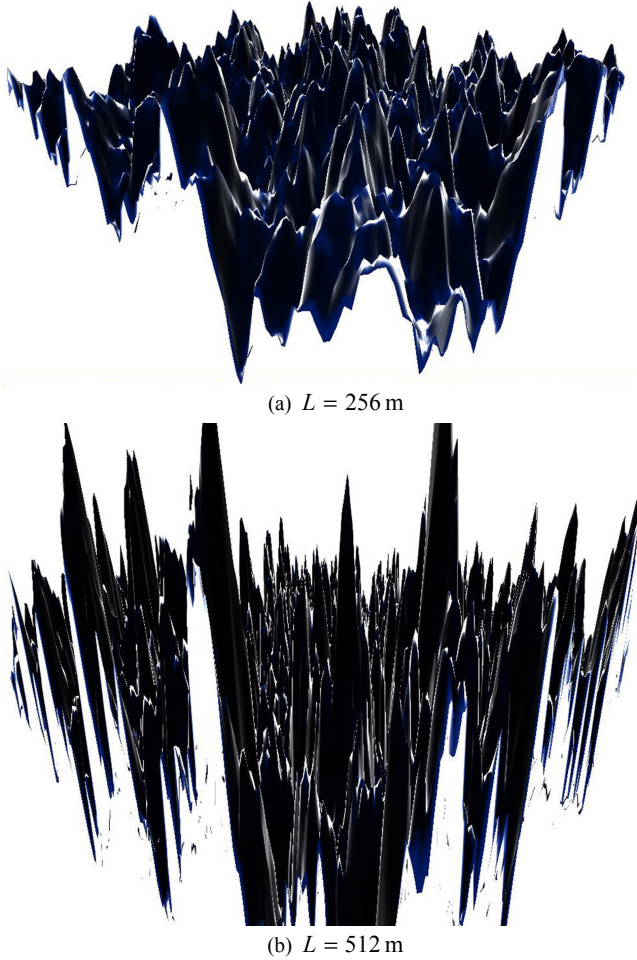


Fig. 1. The generated ocean waves of $\Psi_{ph}(\vec{k})$ ($U_{19.5} = 10.0$ m/s).

III. THE IFFT GERSTNER WAVE

[18] provided the expression of the IFFT Gerstner wave, and [19-30] directly made use of it. However, neither [18] nor [19-30] gave the derivation of the expression. Although [15]

derived the expression of the IFFT Gerstner wave, the work was not complete and had some flaws:

- The IFFT solution of the height field was worked out but lack of some intermediate steps.
- The IFFT solution of the choppy wave was not produced.
- The expression of calculating the amplitude of the cosine wave is not provided.

To solve the flaws, the author need derive the expression of the IFFT Gerstner wave again, and then compare the re-derived expression with the expression of [18].

A. The IFFT Gerstner Wave with the Amplitude of the Cosine Wave

We now build the solution of the height field from a collection of real cosine waves:

$$h(\vec{x}, t) = \sum_{i,j} A_{ij} \cos(\vec{k} \cdot \vec{x} - \omega_k t + \varphi_{ij}). \quad (5)$$

where φ_{ij} is the phase shift, and φ_{ij} is an independent uniform random number from $[0, 2\pi]$. Next we write the cosine in terms of complex exponentials:

$$\begin{aligned} h(\vec{x}_{pq}, t) = & \sum_{i=-n/2+1}^{n/2-1} \sum_{j=-n/2+1}^{n/2-1} \frac{1}{2} \exp[\sqrt{-1}(\vec{x}_{pq} \cdot \vec{k}_{ij})] A_{ij} \\ & \times \exp[\sqrt{-1}(\varphi_{ij} - \omega_k t)] \\ & + \frac{1}{2} \exp[-\sqrt{-1}(\vec{x}_{pq} \cdot \vec{k}_{ij})] A_{ij} \\ & \times \exp[\sqrt{-1}(\omega_k t - \varphi_{ij})]. \end{aligned} \quad (6)$$

We write the cosine in terms of another complex exponentials:

$$\begin{aligned} h(\vec{x}_{pq}, t) = & \sum_{i=-n/2+1}^{n/2-1} \sum_{j=-n/2+1}^{n/2-1} \frac{1}{2} \exp[\sqrt{-1}(\vec{x}_{pq} \cdot \vec{k}_{-i,-j})] A_{-i,-j} \\ & \times \exp[\sqrt{-1}(\varphi_{-i,-j} - \omega_k t)] \\ & + \frac{1}{2} \exp[-\sqrt{-1}(\vec{x}_{pq} \cdot \vec{k}_{-i,-j})] A_{-i,-j} \\ & \times \exp[\sqrt{-1}(\omega_k t - \varphi_{-i,-j})]. \end{aligned} \quad (7)$$

where $\vec{k}_{-i,-j} = -\vec{k}_{ij}$. By comparing expression (6) with (7), we can get the IFFT formula of the height field as:

$$h(\vec{x}_{pq}, t) = \sum_{i=-n/2+1}^{n/2-1} \sum_{j=-n/2+1}^{n/2-1} \tilde{h}(\vec{k}_{ij}, t) \exp[\sqrt{-1}(\vec{x}_{pq} \cdot \vec{k}_{ij})]. \quad (8)$$

where $\tilde{h}(\vec{k}_{ij}, t)$ is the Fourier coefficient. It is expressed as:

$$\begin{aligned} \tilde{h}(\vec{k}_{ij}, t) = & \tilde{h}_0(\vec{k}_{ij}) \exp(-\sqrt{-1}\omega_k t) \\ & + \tilde{h}_0^*(-\vec{k}_{ij}) \exp(\sqrt{-1}\omega_k t). \end{aligned} \quad (9)$$

$\tilde{h}_0(\vec{k}_{ij})$ is express as:

$$\tilde{h}_0(\vec{k}_{ij}) = \frac{1}{2}(\cos \varphi_{ij} + \sqrt{-1} \sin \varphi_{ij}) A_{ij}. \quad (10)$$

We note $\tilde{h}_0(\vec{k}_{ij})$ includes A_{ij} . Therefore, $\tilde{h}(\vec{k}_{ij}, t)$ contains A_{ij} . The above derived IFFT formula of the height field agrees well with that of [15].

The choppy wave is computed as:

$$\mathbf{D}(\vec{x}_{pq}, t) = - \sum_{i=-n/2+1}^{n/2-1} \sum_{j=-n/2+1}^{n/2-1} \frac{\vec{k}_{ij}}{k} A_{ij} \sin(\vec{k}_{ij} \cdot \vec{x}_{pq} - \omega_k t + \varphi_{ij}). \quad (11)$$

The IFFT formula of the choppy wave is:

$$\mathbf{D}(\vec{x}_{pq}, t) = - \sum_{i=-n/2+1}^{n/2-1} \sum_{j=-n/2+1}^{n/2-1} \frac{\vec{k}_{ij}}{k} \tilde{h}_c(\vec{k}_{ij}, t) \exp[\sqrt{-1}(\vec{k}_{ij} \cdot \vec{x}_{pq})]. \quad (12)$$

$\tilde{h}_c(\vec{k}_{ij}, t)$ is the Fourier coefficient of the choppy wave:

$$\begin{aligned} \tilde{h}_c(\vec{k}_{ij}, t) &= \tilde{h}_{c0}(\vec{k}_{ij}) \exp(-\sqrt{-1}\omega_k t) \\ &\quad + \tilde{h}_{c0}^*(-\vec{k}_{ij}) \exp(\sqrt{-1}\omega_k t). \end{aligned} \quad (13)$$

where $\tilde{h}_{c0}(\vec{k}_{ij})$ is defined as;

$$\tilde{h}_{c0}(\vec{k}_{ij}) = (\cos \varphi_{ij} + \sqrt{-1} \sin \varphi_{ij}) \frac{A_{ij}}{2\sqrt{-1}}. \quad (14)$$

So $\tilde{h}_c(\vec{k}_{ij}, t)$ also contains A_{ij} .

B. Approximate Solution of the Amplitude of the Cosine Wave

The relation between the wave number spectrum and the amplitude of the cosine wave is as [36]:

$$\Psi(\vec{k}) = \sum_{i,j} \frac{A_{ij}^2}{2} \delta(\vec{k} - \vec{k}_{ij}). \quad (15)$$

where δ denotes the Dirac function. $\Psi(\vec{k})$ is nonnegative, continuous, bounded, and derivable. One should note that $\Psi(\vec{k})$ represents the wave number spectrum, not only the Phillips spectrum.

The relation among $\text{Var}(h)$, A_{ij} and $\Psi(\vec{k})$ is specialized as [36]:

$$\text{Var}(h) = \frac{1}{2} \sum_{i,j} A_{ij}^2 = \iint_{\vec{k}} \Psi(\vec{k}) d\vec{k}. \quad (16)$$

where $d\vec{k} = dk_x dk_y = k dk d\theta$. Although expression (15) explains the relation between $\Psi(\vec{k})$ and A_{ij} , it is very difficult to be implemented by the computer. To facilitate the computer programming, we need another expression. Accordingly, we discretize $\iint_{\vec{k}} \Psi(\vec{k}) d\vec{k}$ to get the approximate solution of A_{ij} . The boundary value of the discrete integral domain is determined by the sample mode for the wave number

vector in IFFT. The generally used method of the discretization of the definite integral includes the Riemann sums, Trapezoid rule and Simpson rule [37]. We employ the right Riemann sum as:

$$\iint_{\vec{k}} \Psi(\vec{k}) d\vec{k} \approx \sum_{i,j} \Psi(\vec{k}_{ij}) \Delta S_{\vec{k}}. \quad (17)$$

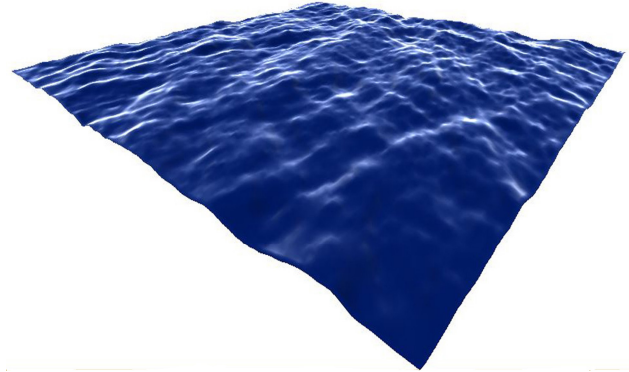
where $\Delta S_{\vec{k}}$ is the area of the discrete integral domain. Let D_{ij} be the discrete integral domain, and $D_{ij} = \{(k_x, k_y) | k_x \in [k_{x,i-1}, k_{x,i}], k_y \in [k_{y,j-1}, k_{y,j}]\}$. Consequently, $\Delta S_{\vec{k}} = \Delta k_x \Delta k_y$, and $\Delta k_x = k_{x,i} - k_{x,i-1} = \Delta k_y = k_{y,j} - k_{y,j-1} = 2\pi / L$. Now we work out the approximate solution of A_{ij} as:

$$A_{ij} = \sqrt{2\Delta S_{\vec{k}}} \Psi(\vec{k}_{ij}). \quad (18)$$

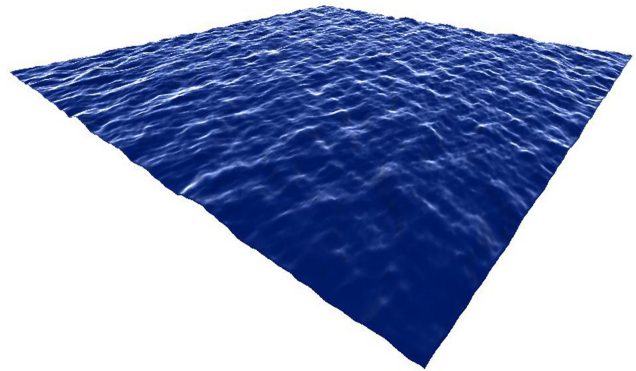
If $\Delta k_x, \Delta k_y \rightarrow 0$, expression (18) turns to expression (15).

Now we get $\tilde{h}_0(\vec{k}_{ij})$ and $\tilde{h}_{c0}(\vec{k}_{ij})$ expressed as:

$$\begin{cases} \tilde{h}_0(\vec{k}_{ij}) = (\cos \varphi_{ij} + \sqrt{-1} \sin \varphi_{ij}) \sqrt{\frac{\Delta S_{\vec{k}}}{2}} \Psi(\vec{k}_{ij}), \\ \tilde{h}_{c0}(\vec{k}_{ij}) = \frac{1}{\sqrt{-1}} (\cos \varphi_{ij} + \sqrt{-1} \sin \varphi_{ij}) \sqrt{\frac{\Delta S_{\vec{k}}}{2}} \Psi(\vec{k}_{ij}). \end{cases} \quad (19)$$



(a) $L = 256$ m



(b) $L = 512$ m

Fig. 2. The generated ocean waves of the method of the paper ($U_{19.5} = 10.0$ m/s).

We respectively substitute the above calculated $\tilde{h}_0(\vec{k}_{ij})$ and $\tilde{h}_0(\vec{k}_{ij})$ in expression (9) and (13), and solve for $\tilde{h}(\vec{k}_{ij}, t)$ and $\tilde{h}_c(\vec{k}_{ij}, t)$, the Fourier coefficient. Both of the coefficients contain $\Delta s_{\vec{k}}$ and $\Psi(\vec{k}_{ij})$.

We employ the Fourier coefficient containing $\Delta s_{\vec{k}}$ and $\Psi(\vec{k}_{ij})$ to render the ocean wave, as shown in Figure 2, and get satisfactory results. As L rises, the wave shape still keeps stable.

IV. COMPARISON STUDIES

A. Comparing the Method in [18] with the Method of the Paper

P is the ocean wave potential per unit area, ρ is the water density, g is the gravity acceleration, and $P = \rho g \text{Var}(h)$. Both ρ and g are constants, so $\text{Var}(h)$ represents the potential. $\text{Var}(h) = \iint_{\vec{k}} \Psi(\vec{k}) d\vec{k}$, and $\Psi(\vec{k})$ is an energy spectrum.

To facilitate comparison, we respectively denote h , \tilde{h} , \tilde{h}_0 and A_{ij} in [18] by h_T , \tilde{h}_T , $\tilde{h}_{0,T}$ and $A_{ij,T}$. In other words, h_T , \tilde{h}_T and $\tilde{h}_{0,T}$ are calculated by expression (1), (2) and (3) respectively. For the Phillips spectrum, if the expression of A includes only $A_{\Psi,ph}$, the wave potential of the method of [18] is:

$$\begin{aligned} \text{Var}[h_T(\vec{x}, t)] &= \sum_{\vec{k}} \text{Var}[\tilde{h}_T(\vec{k}, t) \exp(\vec{k} \cdot \vec{x})] \\ &= \sum_{\vec{k}} [\Psi(\vec{k}) + \Psi(-\vec{k})] = \sum_{\vec{k}} 2\Psi(\vec{k}). \end{aligned} \quad (20)$$

The wave potential of the method of the paper is:

$$\text{Var}[h(\vec{x}, t)] = \sum_{\vec{k}} \Psi(\vec{k}) \Delta s_{\vec{k}}. \quad (21)$$

So $\text{Var}[h_T(\vec{x}, t)]$ does not contain $\Delta s_{\vec{k}}$, but $\text{Var}[h(\vec{x}, t)]$ contains. Consequently we get below expression:

$$\begin{cases} \text{Var}[h(\vec{x}, t)] = \sum_{\vec{k}} \Psi(\vec{k}) \Delta s_{\vec{k}} \approx \iint_{\vec{k}} \Psi(\vec{k}) d\vec{k}, \\ \text{Var}[h_T(\vec{x}, t)] = \sum_{\vec{k}} 2\Psi(\vec{k}_{ij}) \approx \frac{2}{\Delta s_{\vec{k}}} \iint_{\vec{k}} \Psi(\vec{k}) d\vec{k}. \end{cases} \quad (22)$$

where $2/\Delta s_{\vec{k}} = (L/\sqrt{2}\pi)^2$. When the wind velocity is fixed, $\iint_{\vec{k}} \Psi(\vec{k}) d\vec{k}$ is a constant. In above expression, we find the $\text{Var}[h(\vec{x}, t)]$ is accurate, while $\text{Var}[h_T(\vec{x}, t)]$ is overlarge. What is worse, the huger L is, the larger $\text{Var}[h_T(\vec{x}, t)]$ is, and the wave potential of $h_T(\vec{x}, t)$ does not satisfy expression (16). So $\text{Var}[h_T(\vec{x}, t)]$ is miscalculated in this case. This is the reason why the amplitude of the generated ocean wave is malformed in

Figure 1. This also explains why the malformation is turning more serious as L increases.

If the expression of A contains only $A_{\Psi,ph}$, we find that the amplitude of the cosine wave, $A_{ij,T}$, is also miscalculated. Although [18] did not give the expression of $A_{ij,T}$, we can get it by comparison. Expression (3) is written as:

$$\tilde{h}_0(\vec{k}_{ij}) = (\varepsilon_1' + \sqrt{-1\varepsilon_2'}) \sqrt{\Psi(\vec{k}_{ij})}. \quad (23)$$

where $\varepsilon_1' = \varepsilon_1 / \sqrt{2}$, $\varepsilon_2' = \varepsilon_2 / \sqrt{2}$, $E(\varepsilon_1') = E(\varepsilon_2') = 0$ and $\text{Var}(\varepsilon_1') = \text{Var}(\varepsilon_2') = 1/2$. Consequently, ε_1' and ε_2' respectively play the same role as $\cos \varphi_{ij}$ and $\sin \varphi_{ij}$. Comparing expression (23) with (10), we get $A_{ij,T}$ as:

$$A_{ij,T} = 2\sqrt{\Psi(\vec{k}_{ij})}. \quad (24)$$

The expression of $A_{ij,T}$ does not contain $\Delta s_{\vec{k}}$ either, and it is miscalculated. Hence, if L is great (i.e. $\Delta s_{\vec{k}}$ is small), $A_{ij,T} \gg A_{ij}$, and the rendered ocean wave is malformed.

The comparisons of the wave potential and the amplitude of the cosine wave indicate that the expression of A should contain not only $A_{\Psi,ph}$.

If $\text{Var}[h_T(\vec{x}, t)] = \text{Var}[h(\vec{x}, t)]$ and $A_{ij,T} = A_{ij}$, A is expressed as:

$$A = \frac{1}{2} \Delta s_{\vec{k}} A_{\Psi,ph}. \quad (25)$$

Expression (25) shows that the value of A depends on $A_{\Psi,ph}$ as well as $\Delta s_{\vec{k}}$. In this case, both the wave potential and the amplitude of the cosine wave are computed correctly, and the shape of the generated wave is stable.

B. Comparing the Wave Potential of Open Source Codes with That of the Method of the Paper

Some well known open source codes, such as osgOcean, oceanFFT and ftrefracion, use the geometric surface to render the sea surface, i.e. the sea surface has a uniform scale of the geometric surface. So we first calculate the parameters of the geometric surface, such as the amplitude of the cosine wave and the variance of the height field, according the data of the open source code. Further we get the above-mentioned parameters of the sea surface. The aim of the comparison is to look at the difference between the potential calculated by the method of the paper and the potential of the sea surface calculated according to the open source data.

In osgOcean, the height field of the geometric surface equals to the IFFT height field. But in oceanFFT and ftrefracion, the height field of the geometric surface equals to the IFFT height field multiplied by a small factor denoted p_z . The subscripts GS and OS identify the geometric and sea surface of the open

source code respectively. Consequently, L_{GS} , A_{GS} , h_{GS} and $A_{ij,GS}$ are the length, numeric constant of the Phillips spectrum, height field and cosine wave amplitude of the geometric surface. L_{GS} and A_{GS} are given in the code. According to uniform scaling we can get:

$$p_{xyz} = \frac{L_{OS}}{L_{GS}} = \frac{h_{OS}(\vec{x}, t)}{p_z h_{GS}(\vec{x}, t)} = \frac{A_{ij,OS}}{p_z A_{ij,GS}}. \quad (26)$$

where p_{xyz} is the uniform scale factor and $L_{OS} = L$. So

$\text{Var}[h(\vec{x}, t)] / \text{Var}[h_{OS}(\vec{x}, t)]$ is express as:

$$\frac{\text{Var}[h(\vec{x}, t)]}{\text{Var}[h_{OS}(\vec{x}, t)]} = \left(\frac{A_{ij}}{A_{ij,OS}} \right)^2 = \left(\frac{\pi L_{GS}}{p_z L_{OS}^2} \right)^2 \frac{2A}{A_{GS}}. \quad (27)$$

$\text{Var}[h(\vec{x}, t)] / \text{Var}[h_{OS}(\vec{x}, t)]$, $A_{ij} / A_{ij,OS}$ and some concerned parameters of the codes are listed in Table 1.

TABLE 1
 $\text{Var}[h(\vec{x}, t)] / \text{Var}[h_{OS}(\vec{x}, t)]$, $A_{ij} / A_{ij,OS}$ AND CONCERNED PARAMETERS

Open source code	Concerned parameter					$\text{Var}[h(\vec{x}, t)] / \text{Var}[h_{OS}(\vec{x}, t)]$	$A_{ij} / A_{ij,OS}$
	$L_{OS} (L)$	L_{GS}	p_{xyz}	p_z	A_{GS}		
osgOcean	256 m	256.0	1.0	1.0	0.64×10^{-6}	1.64	1.28
oceanFFT	100 m	2.0	50.0	0.5	1.0×10^{-8}	1.10	1.05
fftrefraction	128 m	128.0	1.0	0.1	0.8×10^{-4}	0.52	0.72

In Table 1, A_{ij} and $\text{Var}[h(\vec{x}, t)]$ are close to $A_{ij,OS}$ and $\text{Var}[h_{OS}(\vec{x}, t)]$ respectively. So in the code of osgOcean, oceanFFT and fftrefraction, A_{GS} and p_z are adjusted to treat the amplitude malformation. The methods of adjusting A_{GS} and p_z is as effective as the method of the paper, which confirms the work of the paper.

Figure 3 is the large scale ocean scene rendered with the method of the paper. The ocean surface is constructed by 17×17 patches. The area of the patch is $256\text{m} \times 256\text{m}$, with 128×128 IFFT grids. The program is implemented on a PC with Geforce GTX 460 GPU and Intel Core(TM) 2 Duo CPU, and the frame rate is 70 f/s. If the number of the IFFT grid of each path increases to 256×256 , the frame rate is 49 f/s.



Fig. 3. The large scale ocean scene.

C. Comparing the Method of the Paper with the Method of Directly Using the Gerstner Wave

We compare the method of the paper with the method of directly using the Gerstner wave model in [6, 7, 9-14], and try other types of wave number spectra in this section.

In [6, 7, 9-14], the directional spectrum is applied to calculate the amplitude of the cosine wave. The relation between the directional spectrum and the wave number spectrum is as [36]:

$$\text{Var}(h) = \iint_{\vec{k}} \Psi(\vec{k}) d\vec{k} = \int_{\omega} \int_{\theta} E(\omega, \theta) d\omega d\theta, \quad (28)$$

$$\Psi(\vec{k}) = E[\omega(k), \theta] \frac{d\omega(k)}{k dk}.$$

where $E(\omega, \theta)$ is the directional spectrum, $E(\omega, \theta) = S(\omega)D(\theta)$, $S(\omega)$ is the frequency spectrum and $D(\theta)$ is the directional distribution. The mostly applied $S(\omega)$ in [6, 7, 9-14] includes the P-M and JONSWAP spectra. These two frequency spectra are recommended by ITTC (International Tank Towing Conference) [38]. The widely used $D(\theta)$ is expressed as:

$$D(\theta) = \frac{1}{2\sqrt{\pi}} \frac{\Gamma(n+1)}{\Gamma(n+1/2)} \cos^{2n} \left(\frac{\theta - \alpha}{2} \right). \quad (29)$$

where Γ is the gamma function, and n is a positive integer.

In [6, 7, 9-14], A_{ij} is expressed as:

$$A_{ij} = \sqrt{2E(\omega_i, \theta_j) \Delta s_{\omega, \theta}}. \quad (30)$$

where $\Delta s_{\omega, \theta} = \Delta \omega \Delta \theta$. If expression (19) is used to calculate \tilde{h}_0 , we can get below expression:

$$\text{Var}(h) = \sum_{i,j} \Psi(\vec{k}_{ij}) \Delta s_{\vec{k}} \approx \sum_{i,j} E(\omega_i, \theta_j) \Delta s_{\omega, \theta}. \quad (31)$$

One should note that in expression (31), $\Psi(\vec{k})$ is the corresponding wave number spectrum of $E(\omega, \theta)$, not only represents the Phillips spectrum. So we can arrive at the conclusion that the wave potential of [6, 7, 9-14] is very close to that of the method of the paper. To further prove the conclusion, another two wave number spectra, $\Psi_{PM}(\vec{k})$ and $\Psi_J(\vec{k})$, are constructed and tried.

The frequency spectrum of $\Psi_{PM}(\vec{k})$ is the P-M spectrum, and the directional distribution of $\Psi_{PM}(\vec{k})$ is in the form of expression (29) with $n=1$. $\Psi_{PM}(\vec{k})$ is expressed as:

$$\Psi_{PM}(\vec{k}) = A_{\Psi, PM} \frac{1}{k^4} \exp\left(-\frac{\beta_{PM} g^2}{U_{19.5}^4 k^2}\right) \cos^2\left(\frac{\theta - \alpha}{2}\right). \quad (32)$$

where $A_{\Psi, PM} = \alpha_{PM} / 2\pi$, $\alpha_{PM} = 8.1 \times 10^{-3}$, $\beta_{PM} = 0.74$ [38]. $\Psi_{PM}(\vec{k})$ is the spectrum of the fully developed sea. The rendering results of $\Psi_{PM}(\vec{k})$ is very similar with that of the Phillips spectrum.

The frequency spectrum of $\Psi_J(\vec{k})$ is the JONSWAP spectrum, and the directional distribution of $\Psi_J(\vec{k})$ is the same as that of $\Psi_{PM}(\vec{k})$. $\Psi_J(\vec{k})$ is expressed as:

$$\Psi_J(\vec{k}) = A_{\Psi, J} \frac{1}{k^4} \exp\left(-\frac{5 \omega_{0,J}^4}{4 g^2 k^2}\right) \gamma^{a_J} \cos^2\left(\frac{\theta - \alpha}{2}\right). \quad (33)$$

where $A_{\Psi, J} = \alpha_J / 2\pi$, and $\alpha_J = 0.076 \bar{X}^{-0.22}$ [39],

$$\bar{X} = gX / U_{10}^2, \text{ and } X \text{ is the fetch,}$$

U_{10} is the wind velocity at the height of 10 m above the sea surface,

$\omega_{0,J}$ is the peak frequency of the JONSWAP spectrum, and $\omega_{0,J} = 22(g / U_{10}) \bar{X}^{-0.33}$,

γ is a constant, $1 < \gamma < 7$, with average 3.3;

$$a_J = \exp[-(\omega_k - \omega_{0,J})^2 / (2\sigma^2 \omega_{0,J}^2)],$$

$$\sigma = \begin{cases} 0.07, & \text{if } \omega_k \leq \omega_{0,J} \\ 0.09, & \text{if } \omega_k > \omega_{0,J} \end{cases}.$$

$\Psi_J(\vec{k})$ is used to render the developing sea. Figure 5 is the rendering results of using $\Psi_J(\vec{k})$ in the method of the paper. The shape of the rendered wave is stable.

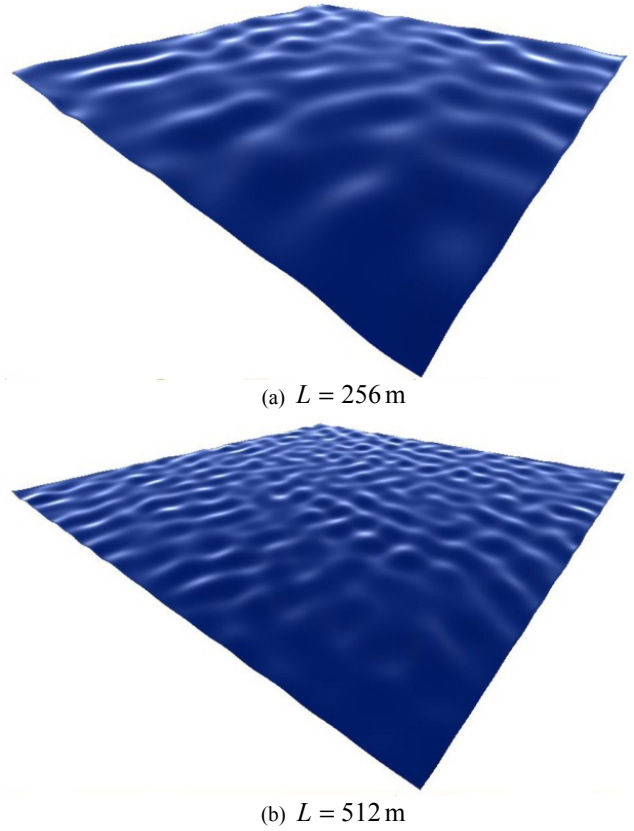


Fig. 5. Rendering results of $\Psi_J(\vec{k})$ ($U_{10} = 11 \text{ m/s}$, $X = 50 \text{ km}$, $\gamma = 3.3$).

V. HOW DO [18-30] GET GOOD RENDERING RESULTS?

Section IV provides the method of A calculating. However, in [18-30], the value of A is not mentioned. If the value of A is not proper, the amplitude of the rendered may be malformed, just as mentioned above. It confuses the author how [18-30] get satisfactory experimental results. The author infers that some factitious methods may be used to suppress the overlarge amplitude and keep wave shape stable. There are two factitious methods:

- Because A is not given, the user of the method can set A very small to keep the generated wave shape stable.
- The other method is to multiply the IFFT height field by a very small factor.

We find the authors of the three open source codes have employed such methods. osgOcean used the first, fftrefraction used the second, and oceanFFT used both. The concerned parameters are listed in Table 1. It is obvious that the code authors have already noticed the phenomenon of the amplitude malformation, but not probed the cause. Although the method is effective, it is only a matter of expediency and lack of basis. The work of the paper gives the method of A calculating, and provides theoretical basis for ocean wave rendering with the IFFT Gerstner wave model.

VI. CONCLUSIONS

Tessendorf [18] raised the model of the IFFT Gerstner wave to render the ocean wave, and [19-30] used the method. [18-30] got good rendering results. However, the value of A , a numeric constant of the Fourier coefficient, is not given in [18-30]. The shape of the rendered ocean wave is under the influence of A . If the value of A is not proper, the amplitude of the generated wave is malformed, and the larger the rendered sea surface, the more serious the malformation. So the author thinks that the method in [18] need be re-examined and the method of A calculating should be provided.

The expression of the IFFT Gerstner wave with the amplitude of the cosine wave is re-derived at first. Then the right Riemann sum is used to discretize the definite integral of the wave number spectrum, and the area of the discrete integral domain is determined by the sample mode for the wave number vector in IFFT. Further we get the expression of the IFFT Gerstner wave, and the Fourier coefficient of the expression contains the wave number spectrum and area of discrete integral domain. The method mentioned above treats the amplitude malformation and keeps the generated wave form stable.

Comparison studies and experiments are done to calculate the value of A and approve the value.

By comparing the expression of the method of the paper with that of [18], we find that the expression of A should contain not only $A_{\Psi,ph}$, the spectral constant of the wave number spectrum of the Phillips spectrum, but also ΔS_k^- , the area of discrete integral domain of the sampled wave number vector. If the expression of A contains only $A_{\Psi,ph}$, the potential of the rendered wave is overlarge, and the amplitude malformation occurs. The larger the width of the rendered sea surface, the more serious the malformation. If the expression of A contains $A_{\Psi,ph}$ and ΔS_k^- , both the wave potential and the amplitude of the cosine wave are correctly calculated, and the shape of the generated wave is stable.

After reading some well known open source codes, including osgOcean, oceanFFT and fftrefraction, we find the code authors take factitious methods to suppress the amplitude malformation, and the wave potential of the suppressed wave is close to that of the method of the paper. It is obviously appeared that the code authors have already noticed the phenomenon of the amplitude malformation, but not discovered the cause. The factitious method is effective, but lack of basis. In the author's opinion, the factitious method is the reason why [18-30] achieve good results.

We compare the method of directly using the Gerstner wave with the method of the paper. In the former method, the directional spectrum is used to calculate the amplitude of the cosine wave. The wave potential of the method is quite close to that of the method of the paper. The P-M and JONSWAP spectra are employed to construct another two wave number spectra respectively. Both shapes of the rendered wave are stable.

The comparisons and experiment results show that the method of the paper can precisely compute the wave potential, and effectively correct the amplitude malformation.

The wave spectrum used in the above mentioned references, either the wave number spectrum or directional spectrum, is the spectrum of the wind sea. So the generated wave is the wind sea. The wind sea spectrum is reasonably accurate for sever states. However, moderated and low sea states are often of combined nature, consisting of both wind sea and sea swell [40]. So the future work may concentrate in the rendering of the mixed wave and the sea swell. The mixed wave includes the wind sea as well as the sea swell. To animate the mixed wave, we may try the two peak spectrum [40, 41]. The swell spectrum [42] can be applied in rendering the sea swell. This work will make the rendered ocean wave more realistic.

REFERENCES

- [1] S. Bruce, "Long crested wave models," *Computer Graphics and Image Processing*, Vol. 12, No. 2, pp. 187-201, Feb. 1980.
- [2] M. Nelson, "Vectorized procedural models for natural terrain: wave and islands in the sunset," *Computer Graphics (ACM)*, Vol. 15, No. 3, pp. 317-324, Aug. 1981.
- [3] A. Osborne, *Nonlinear ocean waves and the inverse scattering transform*. Boston, USA: Academic Press, 2010, pp. 3-10.
- [4] A. Craik, "The origins of water wave theory," *Annual Review of Fluid Mechanics*, Vol. 36, pp. 1-28, Jan. 2004.
- [5] A. Fournier and W. Reeves, "A simple model of ocean waves," *Computer Graphics (ACM)*, Vol. 20, No. 4, pp. 75-84, Aug. 1986.
- [6] S. Thon and D. Ghazanfarpour, "Ocean waves synthesis and animation using real world information," *Computers & Graphics*, Vol. 26, No. 1, pp. 99-108, Feb. 2002.
- [7] J. Fréchet, "Realistic simulation of ocean surface using wave spectra," in *Proceedings of the 1st International Conference on Computer Graphics Theory and Applications (GRAPP' 06)*, Setubal, Portugal, 2006, pp. 76-83.
- [8] E. Darles, B. Crespin, D. Ghazanfarpour, and J. Gonzato, "A survey of ocean simulation in computer graphics," *Computer Graphics Forum*, Vol. 30, No. 1, pp. 43-60, Mar. 2011.
- [9] D. Hingsinger, F. Neyret and M. Cani. "Interactive animation of ocean waves", in *Proceedings of the 1st ACM SIGGRAPH / Eurographics Symposium on Computer Animation (SCA' 02)*, New York, USA, pp. 161-166, 2002.
- [10] E. Darles, B. Crespin, and D. Ghazanfarpour, "Accelerating and enhancing rendering of realistic ocean scenes," in *Full Paper Proceedings of the 15th International Conference in Central Europe on Computer Graphics, Visualization and Computer Vision (WSCG' 07), Part 2*, Plzen, Czech, 2007, pp. 287-294.
- [11] X. Zhao, F. Li, H. Chen, and S. Zhan, "Ocean wave simulation near the seashore," *Journal of Beijing Institute of Technology*, Vol. 18, No. 2, pp. 181-185, Jun. 2009.
- [12] G. Yin, H. Wang, J. Zhang, H. Chen, "Fractal reconciliation for ocean wave simulation," *Journal of Harbin Engineering University*, Vol. 32, No. 11, pp. 1495-1500, Nov. 2011.
- [13] S. Liu and W. Zhang, "Cartoon-style simulation of water coupled with objects," *Simulation Modeling Practice and Theory*, Vol. 32, No. 2, pp. 52-62, Feb. 2013.
- [14] K. Prachumrak and T. Kanchanapornchai. "Real-time interactive ocean wave simulation using multithread," *World Academy of Science, Engineering and Technology*, Vol. 5, pp. 235-238, Aug. 2011.
- [15] R. Bridson, *Fluid simulation for computer graphics*. Wellesley, MA, USA: A K Peters, Ltd., 2008, pp. 187-194.
- [16] D. Wu, X. Zou, K. Dai et al, "Implementation and evaluation of parallel FFT on Engineering and Scientific Computation Accelerator (ESCA) architecture," *Journal of Zhejiang University - Science C (Computers & Electronics)*, Vol. 12, No. 12, pp. 976-989, Dec. 2011.
- [17] J. Lobeiras, M. Amor, and R. Doallo, "FFT implementation on a stream architecture," in *Proceedings of the 19th International Euromicro*

- Conference on Parallel, Distributed, and Network-based Processing (PDP' 11)*, Ayia Napa, Cyprus, 2011, pp. 119-126.
- [18] J. Tessendorf (1999, Aug). Simulating ocean water [Online]. Available: <http://graphics.ucsd.edu/courses/rendering/2005/jdewall/tessendorf.pdf>
- [19] H. Ren, Y. Yin, and Y. Jin, "Realistic rendering of large-scale ocean wave scene," *Journal of Computer-Aided Design and Computer Graphics*, Vol. 12, No. 12, pp. 1617-1622, Dec. 2008.
- [20] C. Christie, E. Gouthas, L. Swierkowski and O. Williams, "Real-time maritime scene simulation for lidar sensors," in *Proceedings of SPIE, Vol. 8015*, Orlando, USA, pp. G1-G12, 2011.
- [21] J. Mitchell. "Real-time synthesis and rendering of ocean water," ATI Research Technical Report, Marlboro, USA, Apr. 2005.
- [22] E. Miandji, M. Sargazi Moghadam, F. Samavati and M. Emadi, "Real-time multi-band synthesis of ocean water with new iterative up-sampling technique," *Visual Computer*, Vol. 25, No. 5-7, pp. 697-705, May. 2009.
- [23] L. Swierkowski, E. Gouthas, C. Christie and O. Williams, "Boat, wake and wave real-time simulation," in *Proceedings of SPIE, Vol. 7031*, San Diego, USA, pp. A1-A12, 2009.
- [24] M. Weerasinghe, D. Sandaruwan, C. Keppitiyagama, and N. Kodikara, "A novel approach to simulate wind-driven ocean waves in the deep ocean," in *Proceedings of the 13th International Conference on Advances in ICT for Emerging Regions (ICTER' 13)*, Colombo, Sri Lanka, pp. 28-37, 2013.
- [25] S. Wang, F. Kang, and D. Wang, "Ocean wave real-time simulation based on adaptive fusion," in *Proceedings of the 32nd Chinese Control Conference (CCC' 13)*, Xi'an, China, pp. 26-28, 2013.
- [26] M. Nielsen, A. Söderström, and R. Bridson, "Synthesizing waves from animated height fields," *ACM Transactions on Graphics*, Vol. 32, No. 1, pp. 2:1-2:9, Jan. 2013.
- [27] Y. Chiu, and C. Chun, "GPU-based ocean rendering," in *Proceedings of the 7th International Conference on Multimedia and Expo (ICME' 06)*, Toronto, Canada, pp. 2125-2128, 2006.
- [28] C. Wang, J. Wu, C. Yen, P. Liu and C. Chen, "Ocean wave simulation in real-time using GPU," in *the 38th International Computer Symposium (ICS' 10)*, Tainan, Taiwan, pp. 419-423, 2010.
- [29] T. Grindstad and R. Rasmussen, "Deep water ocean surface modeling with ship simulation", M. S. Thesis, Dept. Marine Technology, Norwegian University of Science and Technology, Trondheim, Norway, 2011.
- [30] L. Zhang, C. Guo, Y. Tang, M. Lv, Y. Li and J. Zhao. "Real-time and realistic simulation of large-scale deep ocean wave foams based on GPU," *Journal of Computational Information Systems*, Vol. 10, No. 7, pp. 2821-2828, Apr. 2014.
- [31] B. Kim (2009). osgOcean 1. 0. 1 [Online]. Available: <http://code.google.com/p/osgocean/>
- [32] NVIDIA (2013). oceanFFT, examples of CUDA toolkit [Online]. Available: <https://developer.nvidia.com/cuda-toolkit>
- [33] J. Dart (2003). fftrefraction [Online]. Available: <http://www.pudn.com/downloads346/sourcecode/windows/opengl/detail1510268.html>
- [34] O. Phillips. "The equilibrium range in the spectrum of wind-generated waves," *Journal of Fluid Mechanics*, Vol. 4, No. 4, pp. 426-434, Aug. 1958.
- [35] L. Chen, Y. Jin, Y. Yin and H. Ren, "On the wave spectrum selection in ocean wave scene simulation of the maritime simulator," in *Communications in Computer and Information Science, Vol. 402*, pp. 453-465.
- [36] COST Action 714 Working Group 3. *Measuring and analyzing the directional spectrum of ocean waves*. Luxembourg: Office for Official Publications of the European Communities, 2005, pp. 16-20, 40-46.
- [37] M. Weir, J. Hass, and F. Thomas, *Thomas' calculus including second-order differential equations (11th Edition)*, Boston, USA: Pearson Addison - Wesley, 2006, pp. 603-610.
- [38] Specialist Committee on Waves, "Final report and recommendations to the 23rd ITTC," in *Proceedings of the 23rd ITTC, Vol. 2*, Venice, Italy, pp. 545-547, 2002. Available: <http://ittc.name.org/proc23/Waves.pdf>
- [39] Y. Yu and S. Liu. *Random wave and its applications to engineering (4th Edition)*. Dalian, China: Dalian University of Technology Press, 2011, pp. 149-152.
- [40] E. Bitner-Gregersen and O. Hagen, "Directional spreading in two-peak spectrum at the Norwegian continental shelf," in *Proceedings of the 21st International Conference on Offshore Mechanics and Arctic Engineering (OMAE' 02)*, Vol. 2, Oslo, Norway, pp. 547-556, 2002.
- [41] K. Torsethaugen and S. Haver, "Simplified double peak spectral model for ocean waves," in *Proceedings of the 14th International Offshore and Polar Engineering Conference (ISOPE' 04)*, Toulon, France, pp. 76-84, 2004.
- [42] M. Olagnon, K. Kpogo-Nuwoklo. and Z. Guede, "Statistics processing of West Africa wave directional spectra time-series into a climatology of swell events," *Journal of Marine Systems*, Vol. 130, pp. 101 -108, Feb, 2014.

Instruction for Authors

Editorial objectives

In the journal "Electronics", the scientific papers from different fields of electronics and electrical engineering in the broadest sense are published. Main topics are electronics, automatics, telecommunications, computer techniques, power engineering, nuclear and medical electronics, analysis and synthesis of electronic circuits and systems, new technologies and materials in electronics etc. The main emphasis of papers should be on methods and new techniques, or the application of existing techniques in a novel way.

The reviewing process

Each manuscript submitted is subjected to the following review procedures:

- It is reviewed by the editor for general suitability for this publication;
- If it is judged suitable, two reviewers are selected and a double-blind review process takes place;
- Based on the recommendations of the reviewers, the editor then decides whether the particular paper should be accepted as it is, revised or rejected.

Submissions Process

The manuscripts are to be delivered to the editor by e-mail: electronics@etfbl.net.

Manuscripts have to be prepared in accordance with the instructions given in the template for paper preparation that can be found on the journal's web page (www.electronics.etfbl.net).

Authors should note that proofs are not supplied prior to publication and ensure that the paper submitted is complete and in its final form.

Copyright

Articles submitted to the journal should be original contributions and should not be under consideration for any other publication at the same time. Authors submitting articles for publication warrant that the work is not an infringement of any existing copyright and will indemnify the publisher against any breach of such warranty. For ease of dissemination and to ensure proper policing of use, papers and contributions become the legal copyright of the publisher unless otherwise agreed.

ELECTRONICS, VOL. 18, NO. 2, DECEMBER 2014

PAPERS

STRAINED SILICON LAYER IN CMOS TECHNOLOGY.....	63
Tatjana Pešić-Brđanin, Branko L. Dokić	
STUDY ON A COMPOSITE PATCH ANTENNA BASED ON LEFT HANDED MATERIAL WITH NEAR ZERO INDEX.....	70
Jijun Wang, Zhipan Zhu, Yanrong Zhang, Leilei Gong, Yuntuan Fang	
NEW BLOOD LEVEL MEASUREMENT SYSTEM IN BLOOD SEPARATING MACHINE.....	75
Miloš Petković, Miroslav Božić, Dragiša Popović, Darko Todorović, and Goran S. Đorđević	
NEW SINGLE VDCC-BASED EXPLICIT CURRENT-MODE SRCO EMPLOYING ALL GROUNDED PASSIVE COMPONENTS.....	81
Dinesh Prasad, D. R. Bhaskar and Mayank Srivastava	
AMPLITUDE MALFORMATION IN THE IFFT OCEAN WAVE RENDERING UNDER THE INFLUENCE OF THE FOURIER COEFFICIENT.....	89
Lining Chen, Yicheng Jin, and Yong Yin	

ISSN 1450-5843

UDK 621.38